Astronomy & Astrophysics manuscript no. ms
January 7, 2022
©ESO 2022

arXiv:2104.10462v1 [astro-ph.EP] 21 Apr 2021

A transit survey to search for planets around hot subdwarfs: I. methods and performance tests on light curves from Kepler, K2, TESS, and CHEOPS

V. Van Grootel[1], F. J. Pozuelos[1,2], A. Thuillier[1], S. Charpinet[3], L. Delrez[1,2,4], M. Beck[4], A. Fortier[5,6], S. Hoyer[7], S. G. Sousa[8], B. N. Barlow[9], N. Billot[4], M. Dévora-Pajares[10,11], R. H. Østensen[12], Y. Alibert[5], R. Alonso[13,14], G. Anglada Escudé[15,16], J. Asquier[17], D. Barrado[18], S. C. C. Barros[8,19], W. Baumjohann[20], T. Beck[5], A. Bekkelien[4], W. Benz[5,6], X. Bonfils[21], A. Brandeker[22], C. Broeg[5], G. Bruno[23], T. Bárczy[24], J. Cabrera[25], A. C. Cameron[26], S. Charnoz[27], M. B. Davies[28], M. Deleuil[7], O. D. S. Demangeon[8,19], B.-O. Demory[5], D. Ehrenreich[4], A. Erikson[25], L. Fossati[20], M. Fridlund[29,30], D. Futyan[4], D. Gandolfi[31], M. Gillon[2], M. Guedel[32], K. Heng[6,33], K. G. Isaak[17], L. Kiss[34,35,36], J. Laskar[37], A. Lecavelier des Etangs[38], M. Lendl[4], C. Lovis[4], D. Magrin[39], P. F. L. Maxted[40], M. Mecina[32,20], A. J. Mustill[28], V. Nascimbeni[39], G. Olofsson[22], R. Ottensamer[32], I. Pagano[23], E. Pallé[13,14], G. Peter[41], G. Piotto[42,39], J.-Y. Plesseria[43], D. Pollacco[33], D. Queloz[4,44], R. Ragazzoni[42,39], N. Rando[17], H. Rauer[25,45,46], I. Ribas[15,16], N. C. Santos[8,19], G. Scandariato[23], D. Ségransan[4], R. Silvotti[47], A. E. Simon[5], A. M. S. Smith[25], M. Steller[20], G. M. Szabó[48,49], N. Thomas[5], S. Udry[4], V. Viotto[39], N. A. Walton[50], K. Westerdorff[41], and T. G. Wilson[26]

(Affiliations can be found after the references)

Received ...; Accepted...

ABSTRACT

Context. Hot subdwarfs experienced strong mass loss on the Red Giant Branch (RGB) and are now hot and small He-burning objects. Such stars constitute excellent opportunities to address the question of the evolution of exoplanetary systems directly after the RGB phase of evolution.

Aims. In this project we aim to perform a transit survey in all available light curves of hot subdwarfs from space-based telescopes (Kepler, K2, TESS, and CHEOPS), with our custom-made pipeline `SHERLOCK`, in order to determine the occurrence rate of planets around these stars, as a function of orbital period and planetary radius. We also aim to determine whether planets previously engulfed in the envelope of their red giant host star can survive, even partially, as a planetary remnant.

Methods. In this first paper, we perform injection-and-recovery tests of synthetic transits for a selection of representative Kepler, K2 and TESS light curves, to determine which transiting bodies, in terms of object radius and orbital period, we will be able to detect with our tools. We also provide such estimates for CHEOPS data, which we analyze with the `pycheops` package.

Results. Transiting objects with a radius $\lesssim 1.0\ R_\oplus$ can be detected in most of Kepler, K2 and CHEOPS targets for the shortest orbital periods (1 d and below), reaching values as small as $\sim$0.3 $R_\oplus$ in the best cases. Reaching sub-Earth-sized bodies is achieved only for the brightest TESS targets, and the ones observed during a significant number of sectors. We also give a series of representative results for farther and bigger planets, for which the performances strongly depend on the target magnitude, the length and the quality of the data.

Conclusions. The TESS sample will provide the most important statistics for the global aim of measuring the planet occurrence rate around hot subdwarfs. The Kepler, K2 and CHEOPS data will allow us to search for planetary remnants, i.e. very close and small (possibly disintegrating) objects, which would have partly survived the engulfment in their red giant host.

Key words. planet-star interactions; planetary systems; stars: RGB; stars: horizontal branch; stars: subdwarfs; techniques: photometric

1. Introduction

Hot subdwarf B (sdB) stars are hot and compact stars ($T_{\rm eff}$ = 20 000 − 40 000 K and log g = 5.2 to 6.2; Saffer et al. 1994), lying on the blue tail of the horizontal branch (HB), i.e., the extreme horizontal branch (EHB). The HB stage corresponds to core-He burning objects and follows the red giant branch (RGB) phase. Unlike most post-RGB stars that cluster at the red end of the HB (the so-called red clump, RC) because they lose almost no envelope on the RGB (Miglio et al. 2012), sdB stars experienced strong mass loss on the RGB and have extremely thin residual H envelopes ($M_{\rm env} < 0.01 M_\odot$, Heber 1986). This extremely thin envelope explains their high effective temperatures and their inability to sustain H-shell burning. This prevents these stars from ascending the asymptotic giant branch (AGB) after core-He exhaustion (Dorman et al. 1993). About 60% of sdBs reside in binary systems, with about half of them being in close binaries with orbital periods up to a few days (see, e.g., Allard et al. 1994; Maxted et al. 2001), while the other half re-

Send offprint requests to: V. Van Grootel

side in wider binaries with orbital periods up to several years (Stark & Wade 2003; Vos et al. 2018). Binary interactions (through common-envelope -CE- evolution for the short orbits, and stable Roche lobe overflow -RLOF- evolution for the wide orbits) are therefore the main culprit for this extreme mass loss (Han et al. 2002, 2003). The hot O-type subdwarfs, or sdO stars, have $T_{\rm eff}$ = 40 000 − 80 000 K and a wide range of surface gravities. The compact sdO stars (log $g = 5.2 - 6.2$) are either post-EHB objects, or direct post-RGB objects (through a so-called late hot He-flash; Miller Bertolami et al. 2008), or end products of merger events (Iben 1990; Saio & Jeffery 2000, 2002). The sdOs with log g < 5.2 are post-AGB stars, i.e. stars that have ascended the giant branch a second time after core-He burning exhaustion (Reindl et al. 2016).

The formation of the ∼40% of sdB stars that appear to be single has been a mystery for decades. In the absence of a companion, it is hard to explain how the star can expel most of its envelope on the RGB and still achieve core-He burning ignition. Recently, Pelisoli et al. (2020) suggested to all sdB stars might originate from binary evolution. Merger scenarios involving two low-mass white dwarfs have also been investigated (Webbink 1984; Han et al. 2002, 2003; Zhang & Jeffery 2012), but several facts challenge this hypothesis. Firstly, such compact low-mass white dwarf binaries are quite rare, even if some candidates are identified (Ratzloff et al. 2019). Secondly, the mass distribution of single and binary sdB stars are indistinguishable (Fontaine et al. 2012, Table 3 in particular). This mass distribution is mainly obtained from asteroseismology (some sdB stars exhibit oscillations, which allow the precise and accurate determination of the stellar parameters, including total mass; Van Grootel et al. 2013), as well as from binary light curve modeling for hot subdwarfs in eclipsing binary systems. Single and binary mass distributions peak at $\sim 0.47 M_{\odot}$, which is the minimum mass required to ignite He through a He-flash at the tip of RGB (stars of $\gtrsim 2.3 M_{\odot}$ are able to ignite He quietly at lower core masses, down to $\sim 0.33 M_{\odot}$, but the more massive the stars, the rarer they are). A mass distribution of single sdB stars from mergers would on the contrary be much broader (0.4−0.7 $M_{\odot}$; Han et al. 2002). With the DR2 release of *Gaia* (Gaia Collaboration et al. 2018) and precise distances for many hot subdwarfs (Geier 2020), it is also now possible to build a spectrophotometric mass distribution for a much bigger sample compared to what was achieved with the hot subdwarf pulsators or those in eclipsing binaries only. Individual masses are much less precise compared those obtained by asteroseismology or binary light curve modeling (Schneider et al. 2019). However, also here single and binary spectrophotometric mass distributions share the same properties, which tend to discard the hypothesis of different origins for single and binary sdB stars. The third piece of evidence against merger scenarios (that would most likely give fast-rotating objects) is the very slow rotation of almost all single sdB stars, as obtained through $v \sin i$ measurements (Geier & Heber 2012) or from asteroseismology (Charpinet et al. 2018). Moreover, their rotation rates are in direct line with the core rotation rates observed in RC stars (Mosser et al. 2012), which is another strong indication that these stars and the single sdB stars do share a same origin, i.e., they are post-RGB stars.

The question of the evolution of exoplanet systems after the main sequence of their host is generally addressed by studying exoplanets around subgiants, RGB stars and normal HB (RC) stars (hereafter the 'classical' evolved stars). These 'classical' evolved stars are typically very large stars, with radii ranging from $\sim 5-10\ R_{\odot}$ to more than 1000 $R_{\odot}$, much larger than hot subdwarfs with radii in the range $\sim 0.1 - 0.3\ R_{\odot}$ (Heber 2016), and their mass is typically larger than $\sim 1.5\ M_{\odot}$, compared to $\sim 0.47 M_{\odot}$ for hot subdwarfs. Both the transit and radial velocity (RV) methods are challenging for these 'classical' evolved stars due to transit depth dilution and additional noise sources (Van Eylen et al. 2016). Another difficulty for the question of the fate of exoplanet systems after the RGB phase itself is the difficulty on distinguishing RGB and RC stars based on their spectroscopic parameters alone, and sometimes even with help of asteroseismology (Campante et al. 2019). As a consequence, only large/massive planets are detected around the 'classical' evolved stars (Jones et al. 2020, and references therein). A dearth of close-in giant planets is observed around these evolved stars compared to solar-type main sequence stars (Sato et al. 2008; Döllinger et al. 2009). This may be caused by planet engulfment by the host star, but with current technologies it is not possible to determine if smaller planets and remnants (such as the dense core of former giant planets) are present. The lack of close-in giant planets may also be explained by intrinsically different planetary formation for these intermediate-mass stars (see the discussion in Jones et al. 2020). Ultimately, the very existence of planet remnants may be linked to the ejection of most of the envelope on the RGB that occur for hot subdwarfs, while for 'classical' evolved stars, nothing stops the in-spiraling planet inside the host star, and in all cases the planet finally merges with the star, or is fully tidally disrupted, or totally ablated by heating or by the strong stellar wind. In other words, the ejection of the envelope not only makes possible the detection of small objects as remnants, but most importantly may actually be the cause of the existence of such remnants, by stopping the spiraling in the host star.

Many studies focused on white dwarfs (the ultimate fate of ∼97% of all stars), including the direct observations of transiting disintegrating planetesimals (Vanderburg et al. 2015), the accretion of a giant planet (Gänsicke et al. 2019), and, most recently, the transit of a giant planet (Vanderburg et al. 2020). More than 25% of all single white dwarfs exhibit metal pollution in their atmospheres (which should be pure H or He due to gravitational settling of heavier elements in these very high surface gravity objects), which is generally interpreted as accretion of surrounding planetary remnants material (Hollands et al. 2018, and references therein). Statistics on the occurrence rate of planets around white dwarfs as a function of orbital period and planet radius have also been established (Fulton et al. 2014; van Sluijs & Van Eylen 2018; Wilson et al. 2019). However, the vast majority of white dwarfs experienced two giant phases of evolution, namely the RGB and the AGB. The AGB expansion and strong mass loss, followed by the planetary-nebula phase, will have a profound effect on the orbital stability of surrounding bodies (e.g. Debes & Sigurdsson 2002; Mustill et al. 2014; Maldonado et al. 2021). Hence no direct conclusion concerning the effect of RGB expansion alone on the exoplanet systems can be drawn from white dwarfs.

Hot subdwarfs therefore constitute excellent opportunities to address the question of the evolution of exoplanet

systems after the RGB phase of evolution. It is precisely this potential we aim to exploit in this project, by determining the occurrence rate of planets around hot subdwarfs, as a function of orbital period and planet radius. We will achieve this objective by performing a transit search in all available light curves of hot subdwarfs from space-based observatories - such as Kepler (Borucki et al. 2010), K2 (Howell et al. 2014), TESS (Ricker et al. 2014), and CHEOPS (Benz et al. 2020). In this first paper, we provide in Sect. 2 a review of the current status of the search of planets around hot subdwarfs with the different detection methods. We present the observations and the tools used to perform our transit search in Sect. 3. We provide extensive tests of the photometric quality of the light curves in Sect. 4 and 5, and we give our conclusions and future work in Sect. 6.

2. Search for planets around hot subdwarfs: current status

To date, several planet detections around hot subdwarfs have been claimed, but none of them received confirmation. Using the pulsation timing method (variation of the oscillation periods of sdB pulsators), planets of a few Jupiter masses in orbits about 1 AU were announced around V391 Peg and DW Lyn (Silvotti et al. 2007; Lutz et al. 2012), but these claims have recently been refuted (Silvotti et al. 2018; Mackebrandt et al. 2020). Based on weak signals interpreted as reflection and thermal re-emission in Kepler light curves, five very close-in (with orbital periods of a few hours) Earth-sized planets have been claimed to orbit KIC 05807616 (Charpinet et al. 2011) and KIC 10001893 (Silvotti et al. 2014). However, the attribution of such signals to exoplanets is debatable (Krzesinski 2015; Blokesz et al. 2019). Using the RV method, Geier et al. (2009) announced the discovery of a close-in ($P_{\rm orb} = 2.4$ days) planet of several Jupiter masses around HD 149382, but it was ruled out by high-precision RV measurements obtained with the Hobby-Eberly Telescope spectrograph, excluding the presence of almost any substellar companion with $P_{\rm orb} < 28$ days and $M \sin i \gtrsim 1 M_{\rm Jup}$ (Norris et al. 2011). No close massive planets (down to a few Jupiter masses) were found from a mini RV survey carried out with the HARPS-N spectrograph on 8 apparently single hot subdwarfs (Silvotti et al. 2020).

Several ground-based surveys, with both photometric and RV techniques, target the red dwarf or brown dwarf close companions to hot subdwarfs (Schaffenroth et al. 2018, 2019). Such companions are frequent (Schaffenroth et al. 2018), but no Jupiter-like planets have been found to date. In contrast, several discoveries of circumbinary massive planets have been announced in close, post-CE evolution sdB+dM eclipsing systems through eclipse timing variations, e.g. HW Vir, the prototype of the class (Lee et al. 2009; Beuermann et al. 2012), NSVS 14256825 (Zhu et al. 2019), HS 0705+6700 (Pulley et al. 2015), NY Vir (Qian et al. 2012), and 2M 1938+4603 (Baran et al. 2015). Such planets could correspond to first generation, second generation (Schleicher & Dreizler 2014; Völschow et al. 2014), or hybrid planets (which are formed from ejected stellar material accreted on remnants of first generation planets; Zorotovic & Schreiber 2013). Among the ten well studied HW Vir systems, all but one show eclipse timing variations (Heber 2016; Marsh 2018). This may call for another explanation than planets (perhaps something analog to the mechanism suggested for eclipse timing variations in white dwarf binaries; Bours et al. 2016), since the occurrence of circumbinary planets around close main-sequence binaries that are the progenitors of such systems is ∼1% only (Welsh et al. 2012). The properties of the claimed planets often change or are discarded after new measurements (Heber 2016; Marsh 2018), while the orbits are regularly found to be dynamically unstable (e.g. Wittenmyer et al. 2013). None of these claimed circumbinary planets has been confirmed through another technique.

3. Observations and methods

3.1. Space-based light curves of hot subdwarfs

In the original Kepler field, 72 hot subdwarfs were observed at the short cadence (SC) of 1 minute for at least one quarter, including the commissioning quarter Q0 that started on May 2, 2009. During the one-year survey phase that followed Q0 (quarters Q1 of 33.5 days, and Q2 to Q4 of 90 days each, divided in monthly subquarters), 15 sdB stars were found to pulsate (Østensen et al. 2010, 2011). These 15 stars were consequently observed for the rest of the mission at SC (with exceptions of some quarters for a couple of sdB pulsators, see details in Table A.1). Three other sdB pulsators, known as B3, B4 and B5, were found in the open cluster NGC 6791 (Pablo et al. 2011) and were observed in SC for various durations (see Table A.1). Among non-pulsators, 47 hot subdwarfs of the B type (sdB and sdOB) were observed for at least one month at SC (5 of them for several quarters), as well as 7 sdO stars. At the long cadence (LC) of 30 minutes, these 54 non-pulsating hot subdwarfs were generally observed for several quarters, and some of them for the whole duration of the mission. The list of hot subdwarf targets in the original Kepler field and details on the observing quarters in SC and LC can be found in Table A.1. The primary Kepler mission stopped on May 11, 2013 during Q17.2, after the failure of a second reaction wheel necessary to stabilize the spacecraft and obtain the fine and stable pointing for observations of the original field.

The Kepler mission was then redesigned as K2, for which the two remaining reaction wheels allowed a stable pointing for ∼80 days of fields close to the ecliptic. An engineering test of 11 days in February 2014 confirmed the feasibility of this strategy, and 19 campaigns (campaign 0 to 18) were executed from March 2014 to July 2018, when exhaustion of propellants definitively ended the mission. In K2 fields, accounting only for confirmed hot subdwarfs, 39 sdB/sdOB pulsators were observed in SC through at least one campaign. Two more sdB pulsators were discovered through LC data only. 79 more sdB/sdOB non-pulsators, and 10 sdO non-pulsators, were also observed in SC. Finally, 44 hot subdwarfs were observed in LC only. Contrary to Kepler, K2 SC and LC data generally cover one campaign (of about 80 days duration) only, although a few number of stars were observed in two or three campaigns. The full list of hot subdwarfs observed by K2 and details can be found in Table B.1.

TESS (Transiting Exoplanet Survey Satellite) has been operational since July 2018. It is performing a high-precision photometric survey over almost the whole sky (about 90%), avoiding only a narrow band around the ecliptic[1]. The TESS primary two-year mission, which ended

[1] https://tess.mit.edu/observations/

Table 1. Statistics on hot subdwarfs observed in the primary TESS mission (July 2018-July 2020).

Number of sectors	Number of stars
1	877
2	205
3	72
4	23
5	21
6	24
7	7
8	10
9	6
10	6
11	13
12	23
13	15
G magnitude	**Number of stars**
8-9	3
9-10	4
10-11	18
11-12	60
12-13	162
13-14	278
14-15	384
15-16	341
16-17	51
Beyond 17	1

early July 2020, consisted of 26 sectors observed nearly continuously for ∼27.4 days each. Some overlap between sectors exists for the highest northern and southern ecliptic latitudes, hence some stars have been observed for several sectors (see Table 1). The primary mission TESS data products consist of SC observations sampled every 2 minutes for selected stars, as well as full-frame images (FFI) taken every 30 min containing data for all stars in the field of view. Accounting for confirmed hot subdwarfs only, 1302 stars were observed for at least one sector at SC during primary mission. This list was assembled by the Working Group (WG) 8 on compact pulsators of the TESS Asteroseismic Consortium (TASC; see also Stassun et al. 2019). Table 1 presents statistics about these TESS primary mission observations of hot subdwarfs, while the full list can be found at https://github.com/franpoz/Hot-Subdwarfs-Catalogues (see Appendix C for details). The TESS extended mission started on July 4, 2020, and revisits all sectors for the same duration, referred to with increasing numbers (Sector 27, 28, etc.). An 'ultra short cadence' of 20 s is now available in addition to the normal SC of 2 min, and FFIs are now taken every 10 minutes. After release of Sectors 27 to 31, 243 confirmed hot subdwarfs have been observed at 20 s cadence, and 670 more at 2 min cadence (these targets were also selected by WG8 of the TASC). Most of these targets were already observed in the primary mission (sectors 1 to 26), but there are also about one third of new targets that were not observed during the primary mission. The list can be found at https://github.com/franpoz/Hot-Subdwarfs-Catalogues (see Appendix D for details). It is expected that about 2300 hot subdwarfs will have been observed at the end of the two-year extended mission.

CHEOPS (CHaracterising ExOPlanets Satellite) is a European Space Agency (ESA) mission primarily dedicated to the study of known extrasolar planets orbiting bright (6<V<12) stars. It was successfully launched into a 700 km altitude Sun-synchronous 99-min orbit on 18 December 2019. CHEOPS is a 30 cm (effective) aperture telescope optimised to obtain high-cadence high-precision photometric observations for a single star at a time in a broad optical band. CHEOPS is a pointed mission with mostly time-critical observations, so it has ∼20% of free orbits that are partly used to observe bright, apparently single hot subdwarfs as a "filler" program (program ID002). This means that hot subdwarf observations are carried out when CHEOPS has no time-constrained or higher priority observations. The selected targets are generally close to the ecliptic where CHEOPS has its maximum visibility (but were not observed by K2) and are observed for one to three consecutive orbits, for a goal of a total of 18 orbits per target per season. As of December 19, 2020 (8 months after starting the program), 46 hot subdwarf targets have been observed by CHEOPS for a total of 290 orbits. The exposure time is 60 sec for all these targets (except HD 149382, for which it is 41 s). The list of CHEOPS targets and details can be found in Table 2 ("Phase coverage" and "Minimum planet size" columns will be explained in Sect. 5), as well as on https://github.com/franpoz/Hot-Subdwarfs-Catalogues. The nominal duration of the CHEOPS mission is 3.5 years (i.e., end 2023), when we hope to reach a total of about 25-30 orbits on 50-60 targets.

Finally, for completeness, let us mention that the CoRoT satellite (Baglin et al. 2006) performed for ∼24 days a high quality, nearly continuous photometric observation of the sdB pulsator KPD 0629-0016 (Charpinet et al. 2010). We will add these observations in our transit survey, but we will not carry out here a performance test for this one star.

Figure 1 (top) summarizes, ranked per bin of G magnitudes, the available sample of hot subdwarf space-based light curves, as obtained from Kepler, K2, TESS (primary mission, as well as hot subdwarfs observed for the first time in the extended mission), and CHEOPS (as of December 19, 2020). No G magnitude is available for a few Kepler and K2 targets, so they have been included in Fig. 1 with Kp minus 0.1, which is the mean difference between Kp and G magnitudes observed for targets for which both estimates are available. Figure 1 (bottom) shows the celestial distribution of this sample.

3.2. Tools for transit searches in space-based light curves

To search for transit events we will make use of our custom pipeline SHERLOCK (Pozuelos et al. 2020)[2]. This pipeline provides the user with easy access to Kepler, K2 and TESS data, for both SC and LC. The pipeline searches for and downloads the Pre-search Data Conditioning Simple Aperture (PDC-SAP) flux data from NASA's Mikulski Archive for Space Telescope (MAST). Then, it uses a multi-detrend approach via the WOTAN package (Hippke et al. 2019), whereby the nominal PDC-SAP flux light curve is detrended a number of times using a bi-weight filter or a Gaussian process, by varying the window size or the kernel

[2] The SHERLOCK (**S**earching for **H**ints of **E**xoplanets f**R**om **L**ightcurves **O**f spa**C**e-based see**K**ers) code is fully available on GitHub site: https://github.com/franpoz/SHERLOCK

Table 2. List of hot subdwarf targets observed by CHEOPS (as of December 19, 2020).

Name	Type	Gmag	# of orbits (as of 19 Nov 2020)	Phase coverage (days, for >80% coverage)	Min. planet size ($R_\oplus$, for SNR=5 and 0.18$R_\odot$ host)
Active					
HD 149382	sdB	8.80	14 (7x2)	0.47	0.4
HD 127493	sdO	9.96	6.8 (2x1+4.8)	0.18	0.4
TYC981-1097-1	sd	12.01	18 (6x3)	0.68	0.7
Feige 110	sdOB	11.79	6 (3x2)	0.25	0.7
CW83-1419-09	sdOB	12.04	12 (4x3)	0.39	0.7
EC 14248-2647	sdOB	11.98	2 (1x2)	<0.10	0.7
PG 2219+094	sdB	11.90	5 (5x1)	0.18	0.7
PG 1352-023	sdOB	12.06	6 (3x2)	0.18	0.8
LS IV -12 1	sdO	11.11	4 (4x1)	0.18	0.8
Feige 14	sdB	12.77	5 (5x1)	0.11	0.8
EC 22081-1916	sdB	12.94	6 (3x2)	0.25	0.8
LS IV+06 2	He-sdO	12.14	5 (5x1)	0.18	0.8
MCT 2350-3026	sdO	12.07	8 (4x2)	0.32	0.8
TYC 982-614-1	sd	12.21	18 (6x3)	0.68	0.8
EC 20305-1417	sdB	12.34	6 (2x3)	0.25	0.8
LS IV+109	He-sdO	11.97	10 (5x2)	0.39	0.8
PG 1432+004	sdB	12.75	4 (2x2)	0.11	0.8
TonS403	sdO	12.92	11 (11x1)	0.25	0.8
TYC 497-63-1	sdB	12.89	5 (5x1)	0.11	0.8
TYC 999-2458-1	sdB	12.59	3 (1x3)	0.18	0.9
TYC 499-2297-1	sdB	12.63	12 (6x2)	0.54	0.9
LS IV+00 21	sdOB	12.41	4 (2x2)	0.18	0.9
PG 1245-042	sd	13.60	7 (7x1)	0.18	1.0
PG 2151+100	sdB	12.68	9 (3x3)	0.39	1.0
EC 13047-3049	sdB	12.78	2 (1x2)	<0.10	1.0
PG 1505+074	sdB	12.37	2 (2x1)	<0.10	1.0
LS IV -14 116	He-sdOB	12.98	2 (2x1)	0.11	1.0
EC 12578-2107	sdB	13.52	7 (7x1)	0.25	1.0
EC 13080-1508	sdB	13.65	3 (3x1)	0.18	1.0
PB 8783	sdO+F	12.23	6 (3x2)	0.25	1.1
MCT 2341-3443	sdB	10.92	4 (2x2)	0.18	1.1
EC 21595-1747	sdOB	12.62	4 (2x2)	0.18	1.1
PG 1230+067	He-sdOB	13.12	2 (1x2)	0.11	1.1
EC 15103-1557	sdB	12.82	6 (3x2)	0.25	1.1
PG 2313-021	sdB	13.00	6 (3x2)	0.18	1.1
PG 2349+002	sdB	13.27	10 (1x10)	0.32	1.1
PG 1207-033	sdB	13.34	2 (2x1)	0.11	1.1
PG 1303-114	sdB	13.63	5 (5x1)	0.18	1.1
PG 1343-102	sdB	13.69	4 (4x1)	0.25	1.1
Suspended					
LS IV+06 5	sdB	12.37	8 (4x2)	-	>1.3
EC 14338-1445	sdB	13.55	2 (2x1)	-	>1.5
EC 14599-2047	sdB	13.57	3 (3x1)	-	>1.5
EC 01541-1409	sdB	12.27	12 (4x3)	-	>1.5
TYC 1077-218-1	sdOB	12.41	3 (3x1)	-	>2.0
LS IV +09 2	sdB	12.69	4 (2x2)	-	>2.0
TYC 467-3836-1	sdB	11.70	6 (6x1)	-	>2.0

size, respectively. This multi-detrend approach is motivated due to the associated risk of removing transit signals, in particular short and shallow ones. Then, each of the new, detrended light curves, jointly with the nominal PDC-SAP flux, are processed through the TRANSIT LEAST SQUARES package (TLS) (Hippke & Heller 2019) in the search for transits. Contrary to the classical Box Least Square (BLS) algorithm (Kovács et al. 2002), the TLS algorithm uses an analytical transit model that takes the stellar parameters into account. Then, it phase folds the light curves over a range of trial periods (P), transit epochs (T_0), and transit durations (d). It then computes χ^2 between the model and the observed values, searching for the minimum χ^2 value in the 3D-parameter space (P, T_0 and d). It is found that TLS is more reliable than classical BLS in finding any kind of transiting planet, and it is particularly suited for the detection of small planets in long time series, such as these coming from Kepler, K2 and TESS. TLS also allows the user to easily fine-tune the parameters to optimize the search in each case, which is particularly interesting when one deals with shallow transits. In addition, SHERLOCK incorporates a vetting module combining `TPFplotter` (Aller et al. 2020), `LATTE` (Eisner et al. 2020), and `TRICERATOPS` (Giacalone et al. 2021) packages, which allows the user to explore any contamination sources in the photometric aperture used, momentum dumps, background flux variations, x–y centroid positions, aperture size dependencies, flux in-and-out transits, each individual pixel of the target pixel file, and estimate the probabilities for different astrophysical scenarios such as transiting planet, eclipsing binary, eclipsing binary with twice the orbital period, among others. Collectively, these analyses help the user estimate the reliability of a given detection.

For each event that overcomes the vetting process, the user may wish to perform ground- or space-based follow-up observations to confirm the transit event on the target star, which is particularly critical for TESS observations due to the large pixel size (21 arcsec) and point spread function (which could be as large as 1 arcmin). These aspects increase the probability of contamination by a nearby eclipsing binary (see e.g. Günther et al. 2019; Kostov et al. 2019; Quinn et al. 2019; Nowak et al. 2020). However, the results coming directly from the searches performed with SHERLOCK via the TLS algorithm are not optimal; that

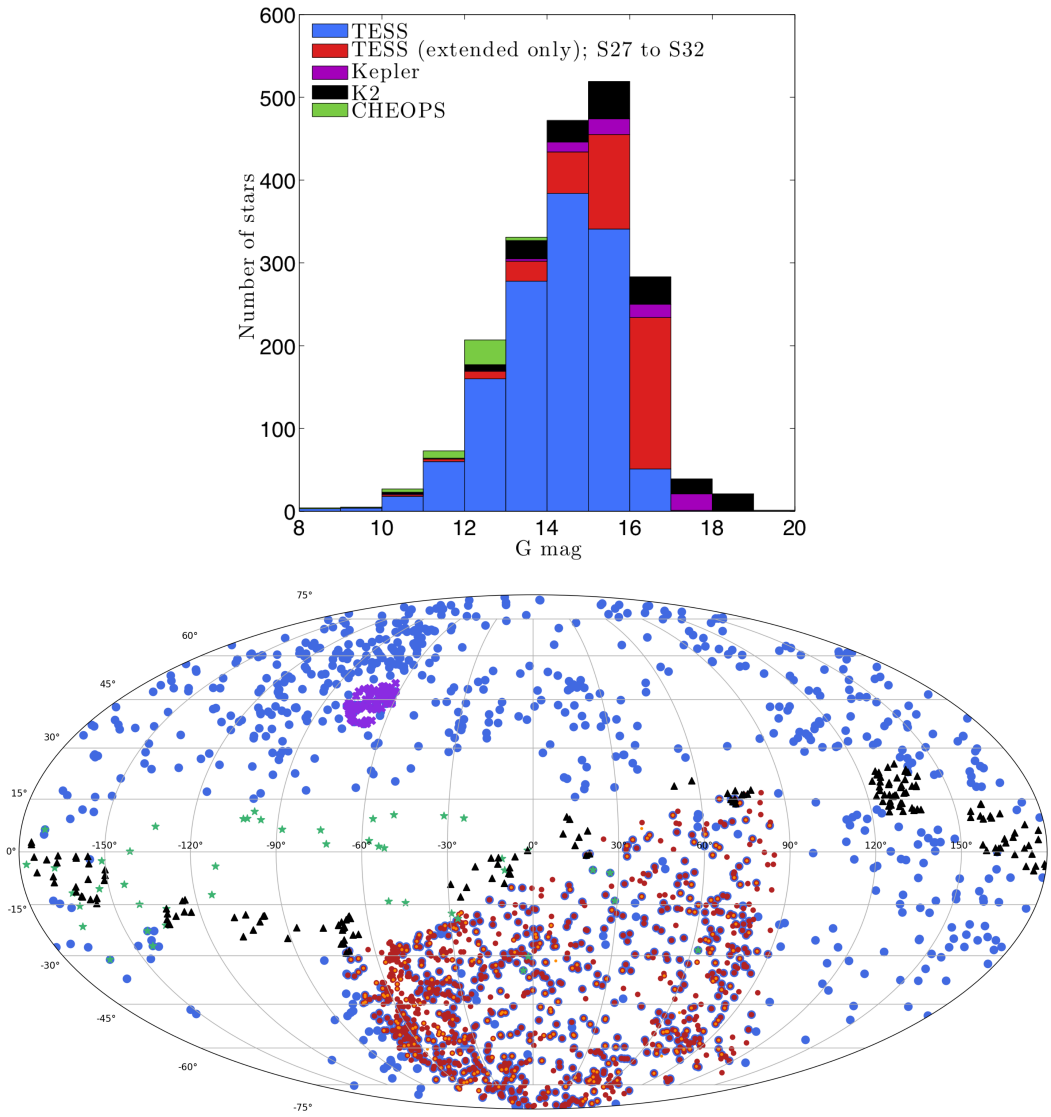


Fig. 1. *Top*: Number of hot subdwarfs per G magnitude bin observed by Kepler, K2, TESS (hot subdwarfs observed in primary mission, which are almost all reobserved in the extended mission), TESS extended only (hot subdwarfs observed for the first time in the extended mission; S27 to S32), and CHEOPS (as of December 19, 2020). *Bottom*: Celestial distribution of these hot subdwarfs: TESS primary mission (blue dots), TESS extended mission 2-min and 20 s (red and dark orange dots), Kepler (purple crosses), K2 (black triangles), and CHEOPS (green stars).

is, the associated uncertainties of P, T_0 and d are large, and their temporal propagation make their use to compute future observational windows and schedule a follow-up campaign impractical. Hence, SHERLOCK uses the results coming from TLS as priors to perform model fitting, injecting them into `allesfitter` (Günther & Daylan 2019, 2020). The user can then choose between Nasted Sampling or MCMC analysis, whose posterior distributions are much more refined, with significant reductions of a few order of magnitudes of the uncertainties of P, T_0 and d. This allows us to schedule a follow-up campaign where the observational windows are more reliable.

4. Injection-and-recovery tests

To quantify the detectability of transiting bodies in our sample of hot subdwarfs, we performed a suite of injection-and-recovery tests. While the detectability of a transit is a target-and-sector/quarter dependent issue, these experiments allow us to verify the general reliability of our survey. We explored several data sets coming from the Kepler, K2 and TESS missions, and for each one we chose a range of stellar magnitudes to study. In all cases, we followed the procedure described by Pozuelos et al. (2020) and Demory et al. (2020); that is, we downloaded the PDC-SAP fluxes in each case and generated a grid of synthetic transiting planets by varying their orbital periods and radii, which are injected in the downloaded light curves. We then detrended the light curves and search for the injected planets. The search itself is done by applying the simple TLS algorithm. Indeed, the multi-detrend approach applied by SHERLOCK makes it more efficient at finding shallow-periodic transits, but with a higher computational cost. Hence, the full use of SHERLOCK in the injection-and-recovery experiments is

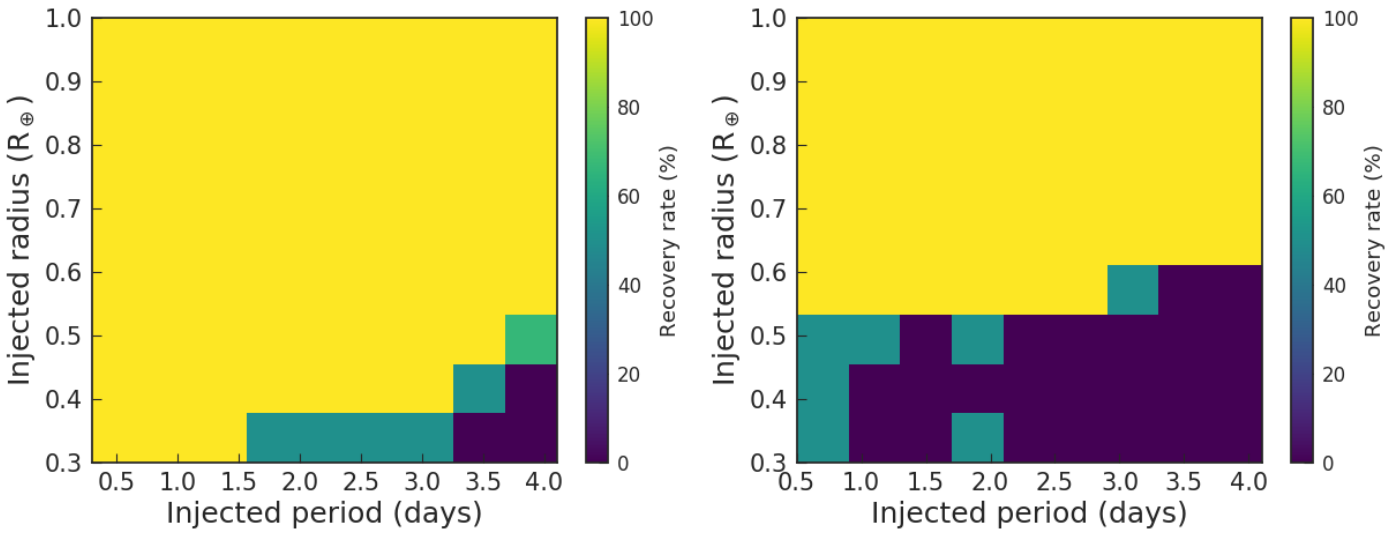


Fig. 2. Injection-and-recovery tests. *Left panel*: KIC 8054179 (Kp=14.40, G=14.34), based on Q6 Kepler data (90 days). *Right panel:* EPIC 206535752 (Kp=13.99, G=14.10), observed during Campaign 3 of K2 (81 days). Injected transits of planets have 0.3-1.0 $R_\oplus$ (steps of 0.1 $R_\oplus$) with 0.5-4.1 d (steps of 0.2 d) orbital periods.

too expensive. That means that our findings in these experiments might be considered as upper limits for the minimum planet sizes, and during our survey we might detect even smaller planets. We defined a synthetic planet as "recovered" when we detect its epoch with one-hour accuracy and if we find its period better than 5%. Depending in the number of sectors/quarters available, we explored the $R_{\rm planet}$–$P_{\rm planet}$ parameter space in different ranges. We conducted two different experiments to qualify the performances achievable with Kepler, K2 and TESS data. The first experiment consisted in full injection-and-recovery tests focusing on a region of the parameter space corresponding to small close-in exoplanets. For Kepler and K2, the injected planets range of 0.3 to 1.0 $R_\oplus$ with steps of 0.1 $R_\oplus$, and 0.5–4.1 d with steps of 0.2 d, for a total of 152 scenarios. For TESS, the injected planets have 0.5–3.0 $R_\oplus$ with steps of 0.05 $R_\oplus$, and 1.0–6.0 d with steps of 0.1 d, hence for a total of 2500 scenarios for each of them. However the 6-sector test, due to computational cost, was done with 0.5–2.5 $R_\oplus$ with steps of 0.2 $R_\oplus$, and 1.0–5.0 d with steps of 0.2 d, for a total of 200 scenarios (as a corollary, injection-and-recovery tests on more sectors, up to 13 sectors for one-year-continuous observations, are out of our reach). The second experiment concerned farther and bigger planets, that is, up to 10.0 $R_\oplus$ and 35 d orbital period. Full injection-and-recovery tests, with sufficiently small steps, led to a too important computational cost. Instead, we chose to focus on particular periods (1, 5, 15, 25 and 35 d), and to determine for these periods what is the minimum planet size detectable for each set of data considered. This limit of 35 d is justified by the transit probability, which quickly falls to very low values with increasing orbital period (for a typical hot subdwarf of 0.15 $R_\odot$ and 0.5 $M_\odot$, the transit probabilities at 10 d and 50 d are about 1% and 0.35% respectively). For each period we explored ∼30 scenarios with fine steps of 0.1 d and 0.1 $R_\oplus$, around a nominal value of the size previously computed with an exploration of sizes from 1 to 10 $R_\oplus$ with steps of 1 $R_\oplus$. This strategy allows us to obtain robust estimations of the sizes with a recovery rate $\gtrsim$ 90% for each period explored, with a total number of scenarios considerably higher than for full injection-and-recovery maps as in Fig. 2–4. The results coming from these experiments are consequently better grounded than those coming from the full maps, which might be considered as more rough estimations of the recovery rates, but with a better and quicker general overview for small and close-in exoplanets. We of course do not exclude to find longer period planets during our transit survey. But for the tests carried out here whose purpose is to quantify our potential to find planets by a transit survey, the limit of 35 d is a good balance between the computational cost and the probability of transit. For Kepler data we explored one quarter, which corresponds to ∼ 90 d of data, as well as monthly subquarters. A similar approach is adopted for K2 data, where observations usually span one campaign of ∼ 80 d of data and sub-samples of 30 d. Finally, for TESS data, we tested data covering 1, 2, 3 and 6 sectors (27 to 162 d).

In all experiments, we assumed that the host star is a canonical hot subdwarf with a radius of 0.175 ± 0.025 $R_\odot$ and a mass of 0.47 ± 0.03 $M_\odot$. We considered only SC data here. We selected targets that are as 'unremarkable' as possible, being non-variable stars (i.e., no peak emerges above 4σ in a Lomb-Scargle periodogram, from pulsations, from reflection/ellipsoidal effect due to a binary nature, or from any other kind of variability) and exhibiting quiet (low scatter) light curves. Indeed, the experiments performed here, based on injection of synthetic transits, apply for computational cost reasons one detrending only to the resulting light curves. In all cases we used the bi-weight method with a nominal window-size of 2.5 h, large enough to protect short transits of close-in exoplanets (which have a typical duration of ∼20 min) and to remove most of the stellar noise, variability and instrumental drifts. For the actual transit search, the light curves will be detrended twelve times using either a bi-weight filter or a Gaussian process (Sect. 3.2), which allows us to optimize the planet search and increasing the detectability of small planets. In this context,

it is therefore important for our injection-and-recovery experiments here to select targets as quiet as possible (minimizing the need of detrending), in order to obtain results as representative as possible.

4.1. Results for Kepler and K2

Figure 2 (left) shows the full injection-and-recovery test for KIC 8054179 (Kp=14.40, G=14.34) from the Q6 Kepler data (90 days). We found that planets smaller than $\sim$0.4 $R_\oplus$ with orbital periods larger than $\sim$1.5 days, and smaller than $\sim$0.5 $R_\oplus$ with orbital periods larger than $\sim$3.2 days, have recovery rates below 50%, i.e., we will most likely be unable to detect them (Fig. 2). For the shortest orbital periods ($\lesssim$ 1.5 d), objects as small as $\sim$ 0.3 $R_\oplus$ are fully recovered[3]. Results from the second experiment focusing on farther and larger planets are presented in Table 3: the smallest planet detectable for 1 d to 35 d increases from 0.3 to 1.2 $R_\oplus$ for KIC 8054179, considering 90 d of data.

We also performed similar experiments for 4 other representative Kepler targets with increasing magnitudes, for one subquarter, i.e., 1 month of data (we also provided results for 1 month data for KIC 8054179, for comparison purposes). Results are presented in Table 3. For a typical Kepler target of 16th G magnitude (see Fig. 1), a sub-Earth size planet of 0.7 $R_\oplus$ can still be detected at 1 d period, and a 2.0 $R_\oplus$ at 15 d period (considering one month data).

Figure 2 (right) shows the full injection-and-recovery test for EPIC 206535752 (Kp=13.99, G=14.10), observed during Campaign 3 of K2 (81 days). We find that $\sim$0.6 $R_\oplus$ planets are fully recovered up to $\sim$ 3 d orbital periods, while the detectability of objects smaller than 0.5 $R_\oplus$ quickly drops below 50% for all orbital periods, meaning that we will likely not be able to detect them. Results from the second experiment on EPIC 206535752 focusing on farther and larger planets are presented in Table 3: the smallest planet detectable for 1 d to 35 d quickly increases from 0.6 to 2.1 $R_\oplus$, considering 80 d of data.

Similar experiments were also carried out for 4 other K2 targets with increasing magnitudes, with a sub-sample of 30 d data. Results are presented in Table 3. For a typical K2 target of 15th G magnitude (see Fig. 1), a sub-Earth size planet of 0.7 $R_\oplus$ can still be detected at 1 d period, as can a 1.9 $R_\oplus$ at 15 d period (considering one month of data).

On a concluding remark, for a given magnitude and data duration, the Kepler performances are significantly superior to the K2 ones, although the K2 targets are generally brighter (Fig. 1 and Table 3). Almost all Kepler targets will allow us to detect transiting objects with a radius $\lesssim$ 1.0 $R_\oplus$, while that is the case for about 2/3 of K2 targets.

4.2. Results for TESS

Figure 3 presents results of injection-and-recovery tests for 4 stars observed in 1 sector by TESS. The four selected stars also are very quiet, non-variable stars. They have magnitudes of G=10.1, G=13.0, G=14.1, and G=15.0. Figure 3 shows that typically, $\sim$0.5 $R_\oplus$ (G$\sim$10.0), $\sim$1.2 $R_\oplus$ (G$\sim$13.0), $\sim$1.9 $R_\oplus$ (G$\sim$14.1), and $\sim$2.7 $R_\oplus$ (G$\sim$15.0) planets can be retrieved from TESS 1-sector light curves for the shortest orbital periods with a $\gtrsim$ 90% recovery rate.

To appreciate the increase of the detectability with multi-sector observations, we performed similar tests on TIC 441713413 (G=13.07) observed in 2 sectors (S16, S23), on TIC 220513363 (G=14.1) observed in 3 sectors (S1, S2, S3), and on TIC 362103375 (G=13.04) observed in 6 sectors (S14, S15, S18, S22, S25, and S26). All stars are compared to results from 1-sector-only tests (S16 for TIC 441713413, S1 for TIC 220513363, and S14 for TIC 362103375). Figure 4 and Table 3 present and compare the results of these experiments. The improvement in detectability from 1 to 2 sectors is barely perceptible, and is noticed only for orbital periods beyond 5 d. This is an important result since the majority of TESS targets were observed for 1-sector only during the primary mission (Table 1), and will be re-observed for another 1-sector in the extended mission. No significant improvement of the detectability obtained from 1-sector primary mission (Fig. 3) is therefore expected with 1 more sector data in the extended mission. The improvement from 1 to 3 sectors (TIC 220513363, see Table 3) and 6 sectors (TIC 362103375, see Fig. 4 and Table 3) is increasingly noticeable: for example, we are now able to reach sub-Earth sized objects up to 25 d with 6 sectors, while it was only possible for orbital period of 1 d (and below) with 1 sector only.

A few more words can be said about the impact of the data length on the minimum detectable radius. In an ideal case, the longer the data set, the smaller the planet that can be detected thanks to the increased number of stacked transits, which improves the statistics and increases the signal-to-noise ratio (SNR). This is directly related to the working procedure of our transit search algorithm (TLS, see Sect. 3.2). However, the real nature of light curves, which always present a level of noise that is impossible to remove, makes that we do not always have a clear improvement when staking more transits. This is in particular the case for the short orbital periods, adding more transits does not always yield a vast improvement, providing there is already a large number of them. This can be noticed in Table 3 for orbital periods of 1 d, for e.g. KIC 8054179, EPIC 206535752, TIC 441713413. For longer orbital periods the effect is stronger, because the increase in the number of stacked transits is relatively more important. For example for the TESS sample, the improvement in the minimum size of planets detectable with an orbital period of 15 d is remarkable when we expand our analysis from 1 sector to 2 (TIC 441713413), 3 (TIC 220513363), and 6 sectors (TIC 362103375).

To finish this section, let us mention that Fig. 2–4 as well as Table 3 also allows us to assess the general reliability of our results for Kepler, K2 and TESS light curves. While the detectability will be (unavoidably) target- (for similar magnitude) and/or sector/quarter- (for similar data length) dependent (and also because of the actual radius of the host star, of course), the general comparison of the tests carried out here gives consistent trends. For example, the results on three different stars with G$\sim$13.0 (TIC 096949372, 362103375 and 441713413) for 1-sector TESS data of three different sectors are globally consistent.

5. CHEOPS performances on hot subdwarfs

Figure 5 displays typical light curves obtained by CHEOPS for four representative targets: (1) HD 149382, one of the

[3] we explicitly checked that the detection rate of planets below $\sim$ 0.3 $R_\oplus$ quickly falls below 50%.

Table 3. Minimum size of planets in units of $R_\oplus$ detectable in typical light curves with a $\gtrsim 90\%$ recovery rate. All stars have 0.175 ± 0.025 $R_\odot$ and 0.47 ± 0.03 $M_\odot$.

Object ID	G Mag	Data length (d)	1 d	5 d	15 d	25 d	35 d
Kepler							
8054179	14.3	90	0.3	0.5	0.8	1.0	1.2
		30	0.5	0.6	1.0	–	–
3353239	15.2	30	0.6	0.8	1.1	–	–
5938349	16.1	30	0.7	1.1	2.0	–	–
8889318	17.2	30	0.9	1.2	2.4	–	–
5342213	17.7	30	1.2	1.7	3.2	–	–
K2							
206535752	14.1	80	0.6	0.8	1.0	1.5	2.1
		30	0.6	0.9	1.6	–	–
211421561	14.9	30	0.7	1.4	1.9	–	–
228682488	16.0	30	1.0	1.4	2.5	–	–
251457058	17.1	30	1.4	2.3	3.4	–	–
248840987	18.1	30	2.1	3.3	5.4	–	–
TESS							
147283842	10.1	27	0.5	0.7	1.5	–	–
362103375	13.0	27	1.0	1.7	2.0	–	–
		162	0.7	0.8	0.9	1.0	1.3
096949372	13.0	27	1.1	1.8	2.0	–	–
441713413	13.1	27	1.3	1.7	2.0	–	–
		54	1.3	1.7	1.9	>10	>10
085400193	14.1	27	1.8	2.3	2.8	–	–
220513363	14.1	27	1.6	1.8	2.7	–	–
		81	1.3	1.6	2.5	3.0	3.0
000008842	15.0	27	2.7	3.2	4.7	–	–

brightest known sdB stars (G=8.9) which was not observed by TESS, Kepler or K2; (2) CW83-1419-09 (G=12.0) and (3) TYC 982-614-1 (G=12.2), which represent typical CHEOPS targets in terms of magnitude; and (4) TYC 499-2297-1, a fainter target of G=12.6, which exceeds CHEOPS' standard specifications. The light curves were processed using version 12 of the Data Reduction Pipeline (DRP; Hoyer et al. 2020).

These light curves were obtained with the aperture that offers the smallest root mean square of variation in count rates, which is generally the `DEFAULT` one (which have a radius of 25 arcsec). Then, we evaluated how the flux was correlated with different parameters such as the time, CHEOPS roll angle, x–y centroids, background, and contamination. This inspection was done with the `pycheops`[4] package (v0.9.6), which is developed specifically for the analysis of CHEOPS data. Hence, we decorrelated the light curves of any unwanted trends, by calculating the Bayesian Information Criteria (BIC) of each combination of trends under the assumption that the combination that induces the lowest BIC best describes any trends. If needed, we also removed outliers. Once the light curves were decorrelated, we visually inspected them in the search for potential transits.

The hot subdwarf observations made by CHEOPS are fillers. This results in light curves spanning 1.5 to 5 hr (with gaps due to Earth occultations and/or passages through the South Atlantic Anomaly, but always with a minimum efficiency of 60% along an orbit, and always less than 100%) separated by several days for a given target. This makes impractical the application of injection-and-recovery tests as conducted in Section 4. Indeed, our injection-and-recovery experiments were done via the TLS transit search tool, which is useful for long time-series observations such as the ones coming from Kepler, K2 or TESS. The power of TLS-based searching relies on the stacking of many transits, which eventually increases the signal-to-noise ratio of a given periodic signal. However, the CHEOPS light curves are short observational data sets, in which we expect to find single transits. Hence, to characterize CHEOPS' performance on hot subdwarfs, we estimated the minimum planet size detectable based on the transit depth that could be detected with a SNR of 5, assuming a transit duration of 20 minutes (which is the typical duration for a $\sim$ 12 h orbital period) and for various typical stellar radii from 0.15 to 0.20 $R_\odot$.

The noise of the light curve is estimated by the `pycheops` package using the scaled noise method. It assumes that the noise in the light curve is white noise with standard error b times the error values provided by the CHEOPS DRP. We then inject transits into the light curve and find the transit depth such that the SNR of the transit depth measurement is 1. The transit model used for this noise estimate includes limb darkening so we define the depth as $D = k^2$ where k is the planet-star radius ratio used to calculate the nominal model. We can use a factor s to modify the transit depth in a nominal model $\mathbf{m_0}$ calculated with approximately the correct depth to pro-

[4] https://github.com/pmaxted/pycheops

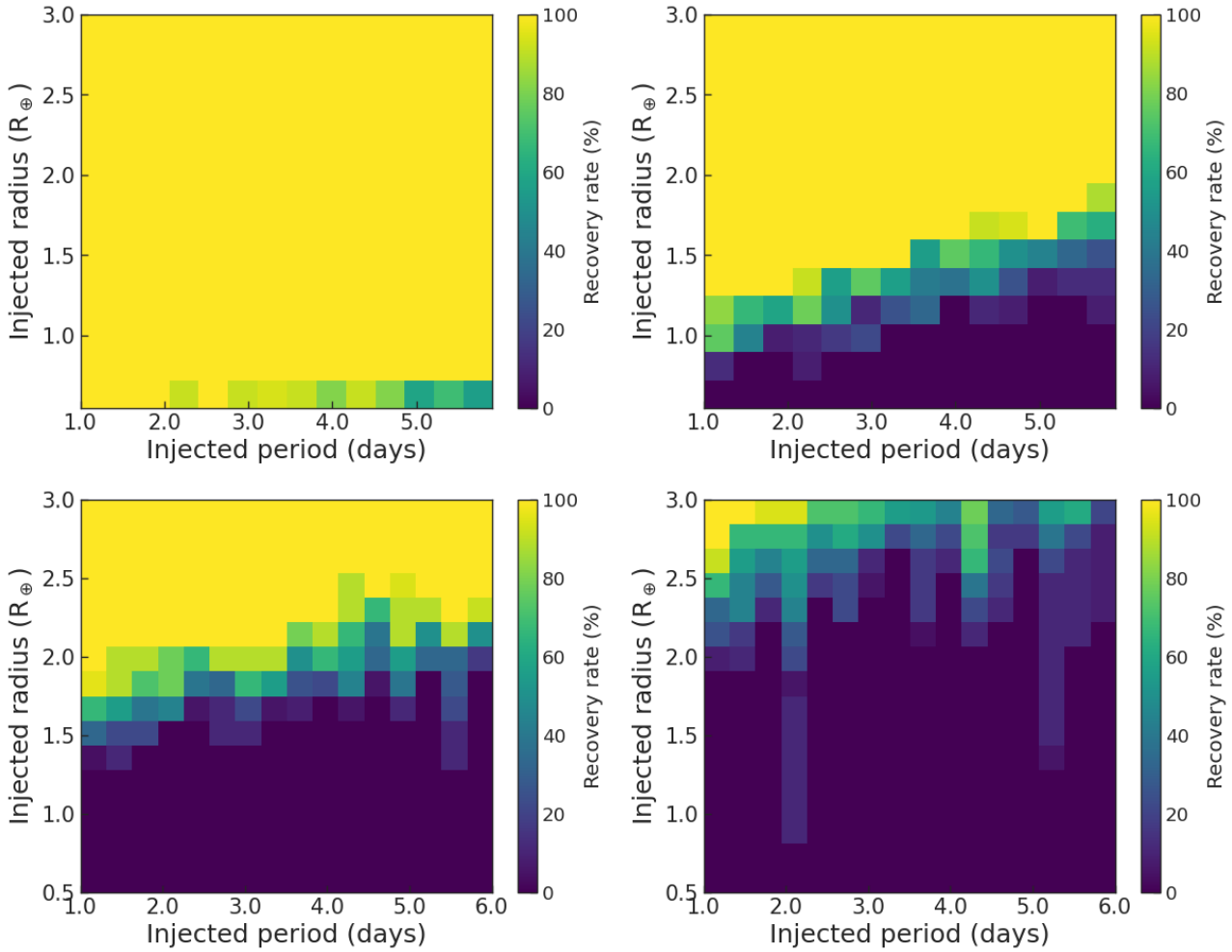


Fig. 3. Results of injection-and-recovery tests on 4 sdB stars observed for one sector by TESS: TIC 147283842 (G=10.1, top left panel), TIC 96949372 (G=13.0, top right panel), TIC 85400193 (G=14.1, bottom left panel), and TIC 000008842 (G=15.0, bottom right panel). 2500 injection-and-recovery tests were made for each star.

duce a new model $\mathbf{m}(s) = 1 + s \times (\mathbf{m_0} - 1)$. If the data are normalised fluxes $\mathbf{f} = f_1, \ldots, f_N$ with nominal errors $\sigma = \sigma_1, \ldots, \sigma_N$ then the log-likelihood for the model given the data is

$$\ln \mathcal{L} = -\frac{1}{2b^2}\chi^2 - \frac{1}{2}\sum_{i=1}^{N} \ln \sigma_i^2 - N \ln b - \frac{N}{2}\ln(2\pi)$$

where $\chi^2 = \sum_i^N \left(f_i - 1 - s(m_{0,i} - 1)\right)^2 / \sigma_i^2$. The maximum likelihood occurs for parameter values $\hat{s}$, and $\hat{b}$ such that $\frac{\partial \ln \mathcal{L}}{\partial s}\big|_{\hat{s},\hat{b}} = 0$ and $\frac{\partial \ln \mathcal{L}}{\partial b}\big|_{\hat{s},\hat{b}} = 0$, from which we obtain

$$\hat{s} = \sum_{i=1}^{N} \frac{(f_i - 1)(m_{0,i} - 1)}{\sigma_i^2} \left[\sum_{i=1}^{N} \frac{(m_{0,i} - 1)^2}{\sigma_i^2}\right]^{-1}$$

and

$$\hat{b} = \sqrt{\chi^2/N}.$$

The standard errors on the eclipse depth if $s \approx 1$ is

$$\sigma_D = Db \left[\sum_{i=1}^{N} \frac{(m_i - 1)^2}{\sigma_i^2}\right]^{-1/2}.$$

Figure 6 shows the minimum planet sizes detectable at SNR=5 for our four representative targets. For HD 149382, a ∼0.4 $R_\oplus$ object (for a 0.18 $R_\odot$ host) could be detected at SNR=5 if transiting. CW83-1419-09 and TYC 982-614-1 exhibit typical results for CHEOPS targets, reaching detections of ∼0.7-0.8 $R_\oplus$ objects. Finally, the fainter TYC 499-2297-1 could allow the detection of a ∼0.9 $R_\oplus$ object. The minimum planet size for all CHEOPS targets can be found in Table 2, which are given for a 0.18 $R_\odot$ host and for SNR=5 in all cases.

Another important property to determine, given the filler nature of CHEOPS observations, is which orbital periods (and for which coverage of the orbit) are reached with the existing observations. This was measured by computing the phase coverage of an hypothetical planet in a range of periods. More precisely, we computed the percentage of the phase covered for each orbital period from $P_{\rm orb}$ =0.001 d to 5 d, in intervals of 0.001 d. Hence, we evaluated the phase coverage for a total of 5000 periods. Then, to aid interpreting the phase coverage at different periods, we binned the periods by 1.7 hr. To illustrate the current status of our observational program, for each target we estimated the period at which a phase coverage of ∼80% is reached, meaning that periods equal to or shorter than this would most likely

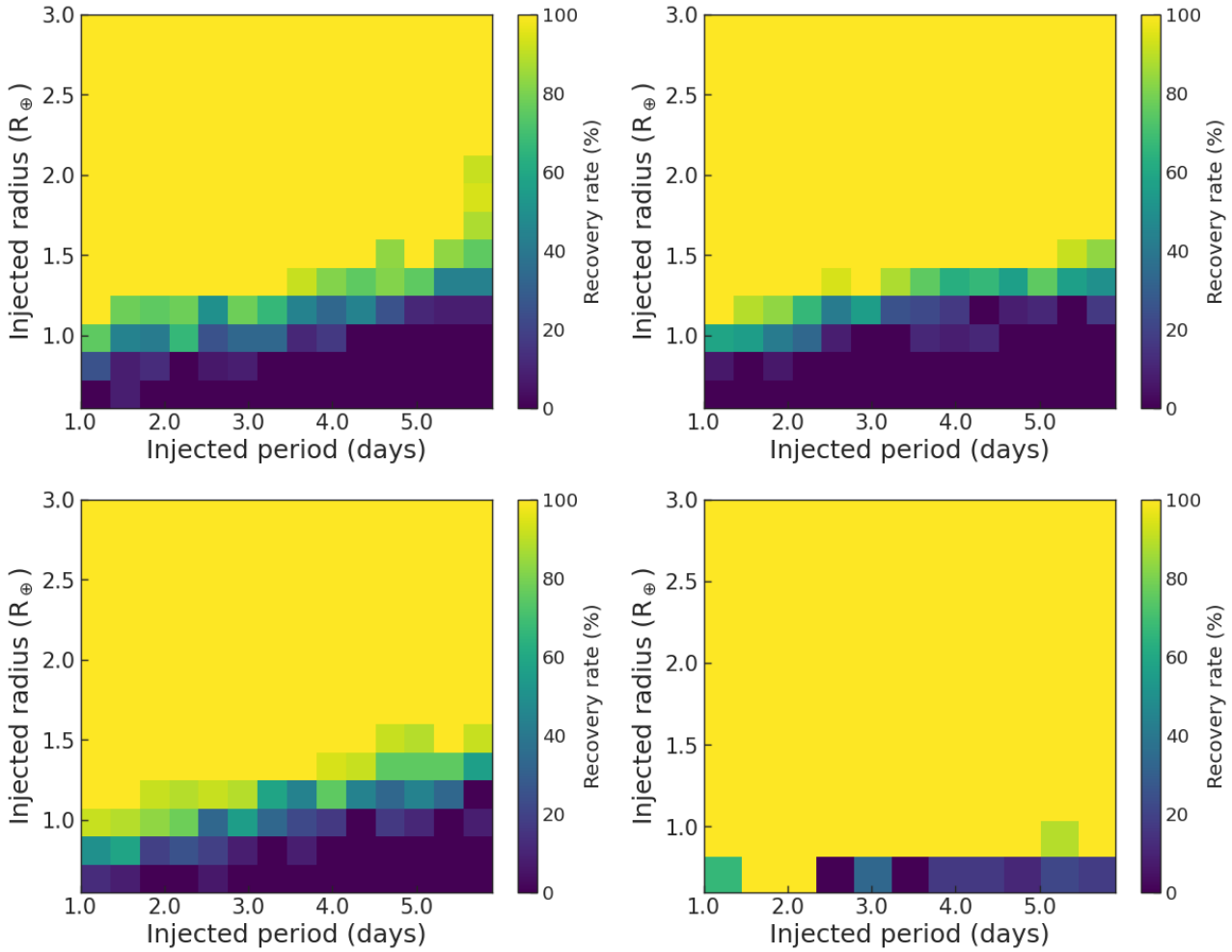


Fig. 4. Results of injection-and-recovery tests on stars observed in multiple sectors by TESS. *Top panels*: TIC 441713413 (G=13.07), 1-sector data (left) and 2-sector data (right). *Bottom panels*: TIC 362103375 (G=13.04), 1-sector data (left) and 6-sector data (right).

be detected if the planet exists and transits. However, even if the probabilities are low, a hypothetical planet may still reside in the unexplored phase. Results for our four representative targets are presented in Fig. 7. As of 19 December 2020, for our four representative cases we found phase coverage of ∼80% for orbital periods of ∼0.47 d, ∼0.39 d, ∼ 0.68 d, and ∼0.54 d for, respectively, HD 149384 (7x2 orbits), CW83 1419-09 (4x3 orbits), TYC 982-614-1 (6x3 orbits), and TYC 499-2297-1 (6x2 orbits). The orbital periods reached for a phase coverage higher than 80% for the CHEOPS targets can be found in Table 2.

In light of the results of the injection-and-recovery tests in the Kepler, K2 and TESS light curves, all CHEOPS targets with a minimum detectable planet size greater than $\gtrsim 1.1 R_\oplus$ have been suspended (see Table 2). These targets generally have fainter magnitudes, or are located in a crowded field, or have a bright close contaminating object, which explains the poorer ability to detect planets around these objects. Another explanation is that some targets are pressure-mode (p-mode) sdB pulsators with a relatively high amplitude (this is the case for EC 15041-1409 and TYC 1077-218-1), which are not properly removed with our current detrending procedure (this is an improvement we aim to implement in the coming months). We instead chose to focus on the most promising targets having planets detectable below $\lesssim 1.1 R_\oplus$, because in these cases, CHEOPS will notably contribute to increasing the number of targets for which we could detect planetary remnants (which are likely small, possibly disintegrating objects) around post-RGB stars. From Tables 1, A.1 and B.1, and the results from Table 3, it is estimated that about 160 stars observed by Kepler and K2 (almost all of them for Kepler, and about 2/3 of them for K2), and about 50 stars from TESS (the very brightest ones, and those with $G \lesssim 13.0$ observed for at least ∼ 6 sectors), will reach this minimum planet size. Statistically only ∼40% of them are single hot subdwarfs, while in contrast, all CHEOPS targets have been chosen to be, to the best of our knowledge, single hot subdwarfs (or, in a few cases, subdwarfs in wide binary systems).

The orbital periods reached by CHEOPS' filler observations will remain modest (about 1 d orbital period with a 80% phase coverage by the end of the mission for most targets). However, these results are valuable for placing constraints on the survival rates of planets that are engulfed in the envelope of their red giant host. Such remnants, if present, are expected to have very short orbital periods due to the orbital decay of orbit of the inspiraling planet inside its host star. It is noteworthy here that

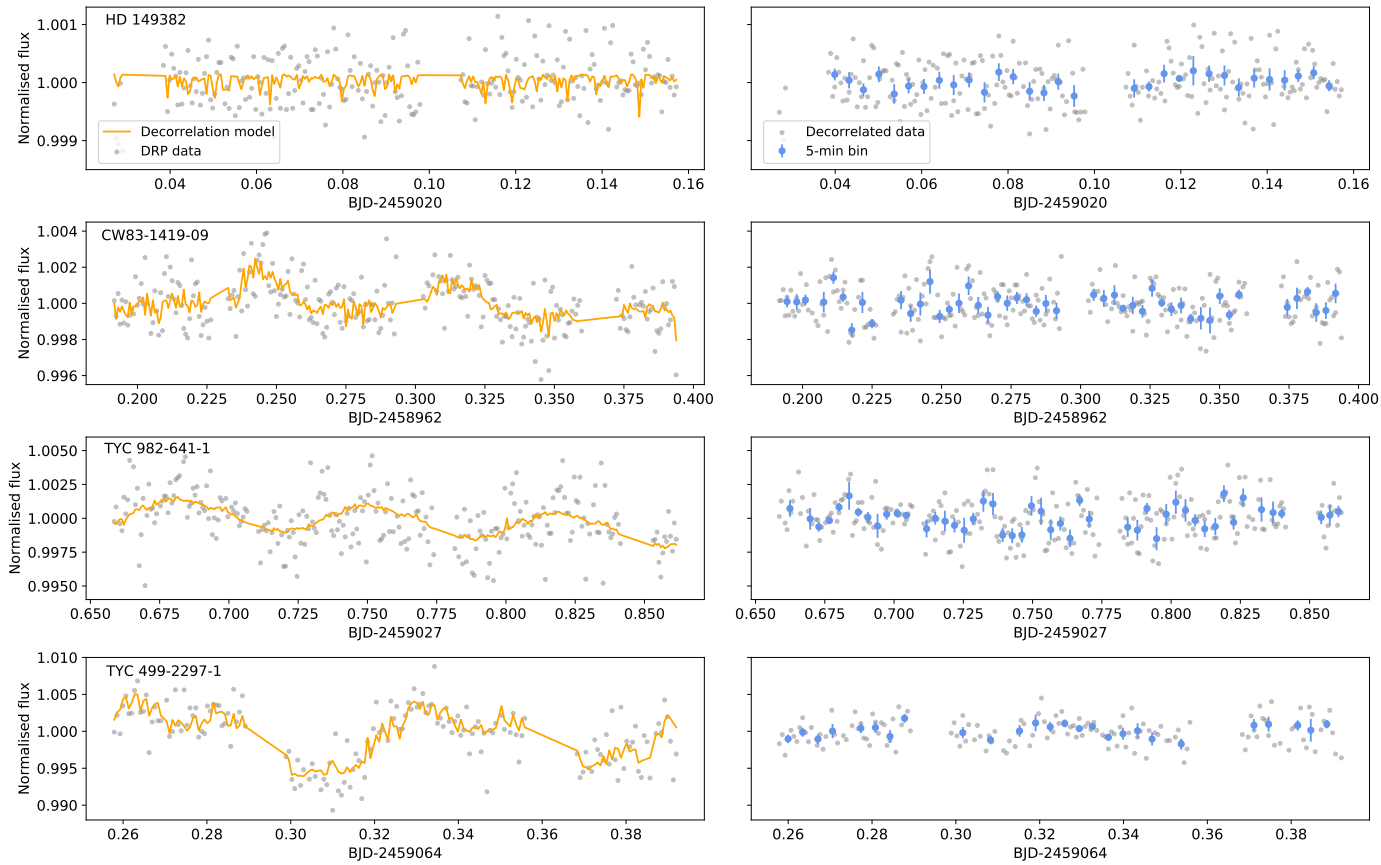


Fig. 5. Representative light curves of hot subdwarfs produced by CHEOPS. From top to bottom: HD 149382 (G=8.9) in its fifth visit, CW83 1419-09 (G=12.0) in its first visit, TYC 982-6141 (G=12.2) in its first visit, and TYC 499-2297-1 (G=12.6) in its fourth visit. In all cases, the raw light curves as processed by the DRP (grey dots) are displayed in the left panels, jointly with the best decorrelation model (orange line) found by means of the `pycheops` package. In the right panels, the decorrelated data (grey dots) with a 5-min bin (blue dots) are shown. The y-scale is the same for each pair of right-and-left panels.

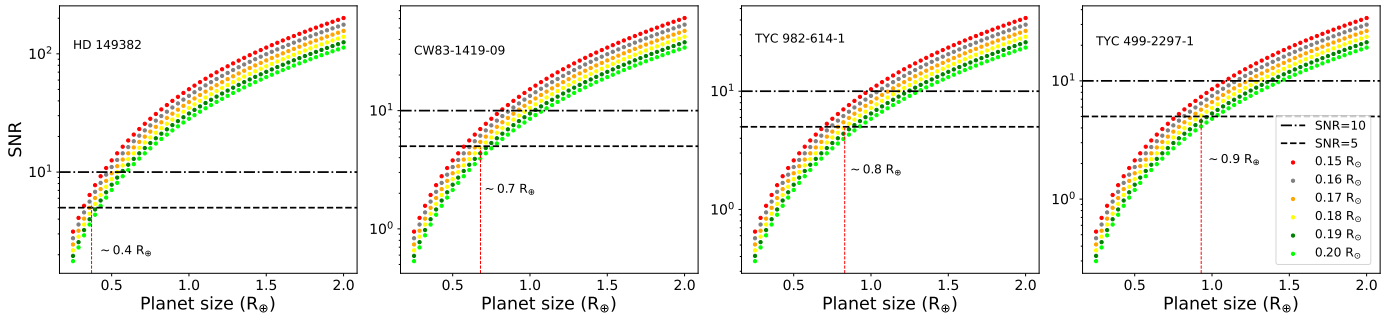


Fig. 6. Performances of CHEOPS on hot subdwarfs, assuming a single 20-min transit. From left to right panel: HD 149382 (G=8.9), CW83-1419-09 (G=12.0), TYC 982-614-1 (G=12.2), and TYC 499-2297-1 (G=12.6). The minimum planet size for SNR=5 and a 0.18 $R_\odot$ host is indicated next to the red vertical line.

all of the five Earth-sized planets suspected around KIC 05807616 and KIC 10001893 have orbital periods of a few hours only; Charpinet et al. 2011; Silvotti et al. 2014, and all known sdB+red dwarf or brown dwarf post-CE binaries have orbital periods below 1 d (Schaffenroth et al. 2018, 2019, 2021). Finally, CHEOPS provides an excellent opportunity to observe very promising targets, such as HD 149382, which have not been observed by Kepler, K2 or TESS.

6. Conclusions and future work

This paper presented our project to perform a transit survey to search for planets around hot subdwarfs. While no such planetary transit have been found to date, high-quality photometric light curves are now available for thousands of hot subdwarfs thanks to the Kepler, K2, TESS and CHEOPS space missions (the harvest is continuing for these last two missions). By having experienced extreme mass loss on the RGB, these small stars (0.1-0.3 $R_\odot$) constitute ex-

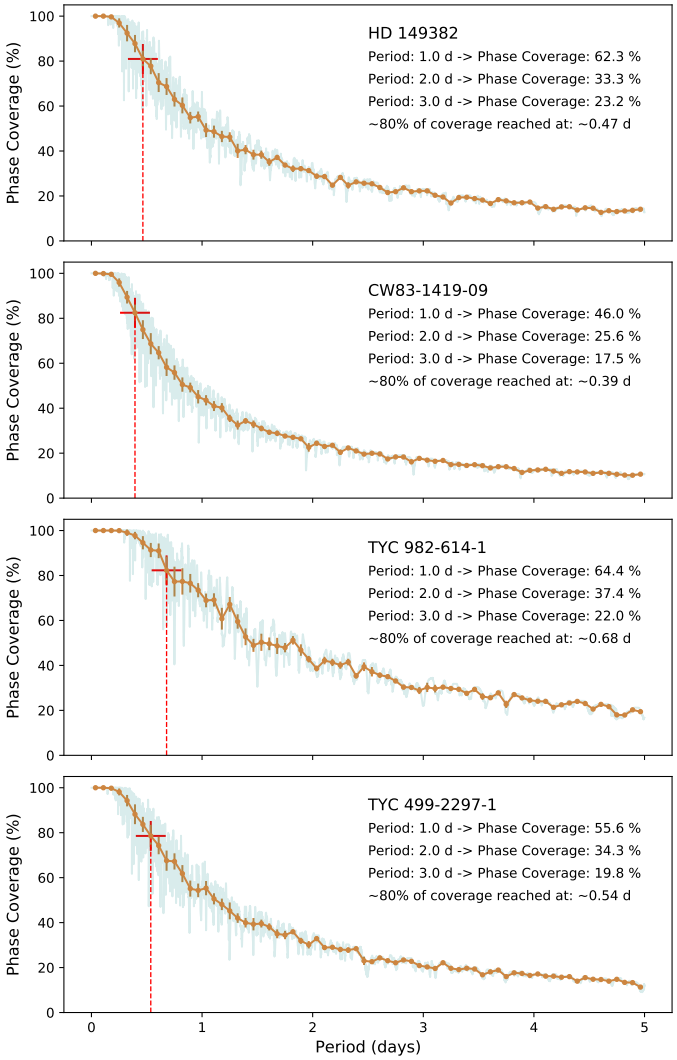


Fig. 7. Phase coverage (in %) as a function of orbital period reached after one season of observations with CHEOPS. From top to bottom panel: HD 149382 (7x2 orbits), CW83 1419-09 (4x3 orbits), TYC 982-614-1 (6x3 orbits), and TYC 499-2297-1 (6x2 orbits). In all cases, the blue lines represent the full range of 5000 periods explored and the orange lines the binning each ~1.7 hr. The orbital periods for which the phase coverages are ~80% are marked with dotted vertical red lines.

cellent targets to address the question of the evolution of planetary systems directly after the first-ascent red giant branch. Hot subdwarfs also offer the potential to observationally constrain the existence of planetary remnants, i.e. planets that would have survived (even partially as a small, possibly disintegrating very close object) the engulfment in the envelope of their red giant host star. Not only does the small star size make possible the detection of small remnant objects, but the ejection of the envelope may actually be the cause of the survival of such remnants, by stopping the spiral-in inside the host star. Hot subdwarfs may therefore offer the outstanding opportunity to study the interior of giant planets, for which the exact structure is uncertain even for Jupiter (Wahl et al. 2017, and refererences therein).

We first listed the hot subdwarfs observed by Kepler, K2, TESS and CHEOPS. We then performed injection-and-recovery tests for a selection of representative targets from Kepler, K2 and TESS, with the aim to determine which transiting bodies, in terms of object radius and orbital period, we will be able to detect in these light curves with our tools. For CHEOPS targets, given the filler nature of the observations (they are carried out when CHEOPS has no time-constrained or higher priority observations), we directly estimated the minimum planet size detectable from the SNR of the light curves, and computed afterwards which orbital periods are covered for a given phase coverage. For comparison purposes, we considered the same host star in all cases.

Objects below $\sim 1 R_\oplus$ size are detectable (if existing and transiting, of course) for the shortest orbital periods (about 1 d and below) in most of Kepler, K2, and CHEOPS targets. Moon-sized values ($\sim 0.3\ R_\oplus$) are achievable in the best cases. Such performance of reaching sub-Earth-sized objects is obtained only for the very few brightest TESS data, as well as for stars with G $\lesssim$ 13 observed for a significant number ($\gtrsim$ 6) of sectors. Altogether, we estimated that for about 250 targets we will be able to detect planets smaller than the Earth for orbital periods below 1 d, should they exist. Given the relatively high probability of transits for very close objects ($\approx$ 5% at 1 d orbital period), our results demonstrate that we will actually be able to observationally determine if planets are able to survive the engulfment in the envelope of their host star. Hot subdwarfs represent a short phase of stellar evolution ($\sim$ 150 Myr for the core-He burning, i.e. EHB, phase, and about 10% of that time for post-EHB evolution; Heber 2016), which renders unlikely the formation of second-generation planets, in particular in light of the harsh environment for planet formation around a hot subdwarf. Migration of farther bodies that were not engulfed in the envelope of the red giant host would be possible for the oldest hot subdwarfs (Mustill et al. 2018), although such a lifetime is likely too short for a complete circularization of the orbit. Dedicated computations will be needed, as carried out for the planets and remnants discovered around white dwarfs (Veras & Fuller 2020, and references therein).

Our tests also provided a series of representative results for the detection of farther and bigger planets. TESS targets will provide the most important cohort to the final goal of this project, which is to provide statistically significant occurrence rates of planets, as a function of object radius and orbital period, around hot subdwarfs.

Our main pipeline for the search for transit events around hot subdwarfs, SHERLOCK, has already been successfully applied in a number of cases (Pozuelos et al. 2020; Demory et al. 2020). However, there are several implementations under development which are especially relevant given the nature of our targets. The first improvement involves more efficient detrending for pulsating stars (see e.g. Sowicka et al. 2017), in particular high-frequency p-mode hot subdwarf pulsators, which have relatively high amplitudes that can hinder the detection of shallow transits. Secondly, we are including in SHERLOCK a model for comet-like tails of disintegrating exoplanets, which highly differ from the typical shape of transiting exoplanets (see e.g. Brogi et al. 2012; Rappaport et al. 2012; Sanchis-Ojeda et al. 2015; Kennedy et al. 2019).

In case of identified transit event in the light curves successfully passing all the thresholds and the vetting process, we will need to confirm the signal and associate it to a planetary nature by scheduling follow-up observations. In order to confirm transit events in light curves, we will trigger for

the deepest signals ($\gtrsim$ 2500 ppm) observations with our Liège TRAPPIST network (Jehin et al. 2011; Gillon et al. 2011), which consists in two 0.6-m telescopes, at the La Silla (Chile) and Oukaïmeden (Morocco) observatories. For shallower transits we will directly use CHEOPS, provided the target has a sufficient visibility from the CHEOPS orbit. Once transits are confirmed, it will be necessary to discard a stellar, white dwarf or brown dwarf origin from RV measurements. We will first search for RV data in archives, open to the community (such as the ESO archives), or within the hot subdwarf community. We will write proposals on appropriate spectrographs when necessary.

Finally, we will compute the occurrence rates of planets around hot subdwarfs by following a method similar to van Sluijs & Van Eylen (2018); Wilson et al. (2019). By comparing our results to these statistics for white dwarfs, to those for ∼0.8-2.3 $M_{\odot}$ main sequence stars that are the main progenitors of hot subdwarfs (e.g. Mayor et al. 2011; Howard et al. 2012; Fressin et al. 2013), as well as for subgiants and RGB stars (Sato et al. 2008; Döllinger et al. 2009; Jones et al. 2020), we will be able to appreciate the effect of the RGB phase alone on the evolution of exoplanetary systems.

Acknowledgements. We thank the anonymous referee for comments that improved the manuscript. The authors thank the Belgian Federal Science Policy Office (BELSPO) for the provision of financial support in the framework of the PRODEX Programme of the European Space Agency (ESA) under contract number PEA 4000131343. This work has been supported by the University of Liège through an ARC grant for Concerted Research Actions financed by the Wallonia-Brussels Federation. The authors acknowledge support from the Swiss NCCR PlanetS and the Swiss National Science Foundation. V.V.G. is a F.R.S.-FNRS Research Associate. M.G. is an F.R.S.-FNRS Senior Research Associate. St.C. acknowledges financial support from the Centre National d'Études Spatiales (CNES, France) and from the Agence Nationale de la Recherche (ANR, France) under grant ANR-17-CE31-0018. K.G.I. is the ESA CHEOPS Project Scientist and is responsible for the ESA CHEOPS Guest Observers Programme. She does not participate in, or contribute to, the definition of the Guaranteed Time Programme of the CHEOPS mission through which observations described in this paper have been taken, nor to any aspect of target selection for the programme. D.E. has received funding from the European Research Council (ERC) under the European Union's Horizon 2020 research and innovation programme (project Four Aces; grant agreement No 724427). This project has been carried out in the frame of the National Centre for Competence in Research PlanetS supported by the Swiss National Science Foundation (SNSF). G.B. acknowledges support from CHEOPS ASI-INAF agreement n. 2019-29-HH.0. A.J.M. acknowledges funding from the Swedish Research Council (starting grant 2017-04945) and the Swedish National Space Agency (career grant 120/19C). A.C.C. and T.G.W. acknowledge support from STFC consolidated grant number ST/M001296/1. A.B. was supported by the SNSA. M.F. gratefully acknowledge the support of the Swedish National Space Agency (DNR 65/19, 174/18). S.H. acknowledges CNES funding through the grant 837319. S.C.C.B. acknowledges support from FCT through FCT contracts nr. IF/01312/2014/CP1215/CT0004. S.G.S. acknowledge support from FCT through FCT contract nr. CEECIND/00826/2018 and POPH/FSE (EC). This work was supported by FCT - Fundação para a Ciência e a Tecnologia through national funds and by FEDER through COMPETE2020 - Programa Operacional Competitividade e Internacionalização by these grants: UID/FIS/04434/2019; UIDB/04434/2020; UIDP/04434/2020; PTDC/FIS-AST/32113/2017 & POCI-01-0145-FEDER- 032113; PTDC/FIS-AST/28953/2017 & POCI-01-0145-FEDER-028953; PTDC/FIS-AST/28987/2017 & POCI-01-0145-FEDER-028987. O.D.S.D. is supported in the form of work contract (DL 57/2016/CP1364/CT0004) funded by national funds through FCT. B.-O.D. acknowledges support from the Swiss National Science Foundation (PP00P2-190080). B.N.B. acknowledges funding through the TESS Guest Investigator Program Grant 80NSSC21K0364. We acknowledge support from the Spanish Ministry of Science and Innovation and the European Regional Development Fund through grants ESP2016-80435-C2-1-R, ESP2016-80435-C2-2-R, PGC2018-098153-B-C33, PGC2018-098153-B-C31, ESP2017-87676-C5-1-R, MDM-2017-0737 Unidad de Excelencia "María de Maeztu"- Centro de Astrobiología (INTA-CSIC), as well as the support of the Generalitat de Catalunya/CERCA programme. The MOC activities have been supported by the ESA contract No. 4000124370. I.R. acknowledges support from the Spanish Ministry of Science and Innovation and the European Regional Development Fund through grant PGC2018-098153-B- C33, as well as the support of the Generalitat de Catalunya/CERCA programme. X.B., Se.C., D.G., M.F. and J.L. acknowledge their role as ESA-appointed CHEOPS science team members. D.G. gratefully acknowledges financial support from the CRT foundation under Grant No. 2018.2323 "Gaseous or rocky? Unveiling the nature of small worlds". P.F.L.M. acknowledges support from STFC research grant number ST/M001040/1. This project has been supported by the Hungarian National Research, Development and Innovation Office (NKFIH) grants GINOP-2.3.2-15-2016-00003, K-119517, K-125015, and the City of Szombathely under Agreement No. 67.177-21/2016. This paper includes data collected by the TESS mission. Funding for the TESS mission is provided by the NASA Explorer Program. Funding for the TESS Asteroseismic Science Operations Centre is provided by the Danish National Research Foundation (Grant agreement no.: DNRF106), ESA PRODEX (PEA 4000119301) and Stellar Astrophysics Centre (SAC) at Aarhus University. We thank the TESS team and staff and TASC/TASOC for their support of the present work. This work has made use of data from the ESA mission Gaia (https://www.cosmos.esa.int/gaia), processed by the Gaia Data Processing and Analysis Consortium (DPAC, https://www.cosmos.esa.int/web/gaia/dpac/consortium). Funding for the DPAC has been provided by national institutions, in particular the institutions participating in the Gaia Multilateral Agreement.

References

Allard, F., Wesemael, F., Fontaine, G., Bergeron, P., & Lamontagne, R. 1994, AJ, 107, 1565
Aller, A., Lillo-Box, J., Jones, D., Miranda, L. F., & Barceló Forteza, S. 2020, A&A, 635, A128
Baglin, A., Auvergne, M., Boisnard, L., et al. 2006, in 36th COSPAR Scientific Assembly, Vol. 36, 3749
Baran, A. S., Zola, S., Blokesz, A., Østensen, R. H., & Silvotti, R. 2015, A&A, 577, A146
Benz, W., Broeg, C., Fortier, A., et al. 2020, Experimental Astronomy [arXiv:2009.11633]
Beuermann, K., Dreizler, S., Hessman, F. V., & Deller, J. 2012, A&A, 543, A138
Blokesz, A., Krzesinski, J., & Kedziora-Chudczer, L. 2019, A&A, 627, A86
Borucki, W. J., Koch, D., Basri, G., et al. 2010, Science, 327, 977
Bours, M. C. P., Marsh, T. R., Parsons, S. G., et al. 2016, MNRAS, 460, 3873
Brogi, M., Keller, C. U., de Juan Ovelar, M., et al. 2012, A&A, 545, L5
Campante, T. L., Corsaro, E., Lund, M. N., et al. 2019, ApJ, 885, 31
Charpinet, S., Fontaine, G., Brassard, P., et al. 2011, Nature, 480, 496
Charpinet, S., Giammichele, N., Zong, W., et al. 2018, Open Astronomy, 27, 112
Charpinet, S., Green, E. M., Baglin, A., et al. 2010, A&A, 516, L6
Debes, J. H. & Sigurdsson, S. 2002, ApJ, 572, 556
Demory, B. O., Pozuelos, F. J., Gómez Maqueo Chew, Y., et al. 2020, A&A, 642, A49
Döllinger, M. P., Hatzes, A. P., Pasquini, L., Guenther, E. W., & Hartmann, M. 2009, A&A, 505, 1311
Dorman, B., Rood, R. T., & O'Connell, R. W. 1993, ApJ, 419, 596
Eisner, N., Lintott, C., & Aigrain, S. 2020, The Journal of Open Source Software, 5, 2101
Fontaine, G., Brassard, P., Charpinet, S., et al. 2012, A&A, 539, A12
Fressin, F., Torres, G., Charbonneau, D., et al. 2013, ApJ, 766, 81
Fulton, B. J., Tonry, J. L., Flewelling, H., et al. 2014, ApJ, 796, 114
Gaia Collaboration, Brown, A. G. A., Vallenari, A., et al. 2018, A&A, 616, A1
Gänsicke, B. T., Schreiber, M. R., Toloza, O., et al. 2019, Nature, 576, 61
Geier, S. 2020, A&A, 635, A193
Geier, S., Edelmann, H., Heber, U., & Morales-Rueda, L. 2009, ApJ, 702, L96
Geier, S. & Heber, U. 2012, A&A, 543, A149

Giacalone, S., Dressing, C. D., Jensen, E. L. N., et al. 2021, AJ, 161, 24
Gillon, M., Jehin, E., Magain, P., et al. 2011, in European Physical Journal Web of Conferences, Vol. 11, European Physical Journal Web of Conferences, 06002
Günther, M. N. & Daylan, T. 2019, Allesfitter: Flexible Star and Exoplanet Inference From Photometry and Radial Velocity, Astrophysics Source Code Library
Günther, M. N. & Daylan, T. 2020, arXiv e-prints, arXiv:2003.14371
Günther, M. N., Pozuelos, F. J., Dittmann, J. A., et al. 2019, Nature Astronomy, 3, 1099
Han, Z., Podsiadlowski, P., Maxted, P. F. L., & Marsh, T. R. 2003, MNRAS, 341, 669
Han, Z., Podsiadlowski, P., Maxted, P. F. L., Marsh, T. R., & Ivanova, N. 2002, MNRAS, 336, 449
Heber, U. 1986, A&A, 155, 33
Heber, U. 2016, PASP, 128, 082001
Hippke, M., David, T. J., Mulders, G. D., & Heller, R. 2019, AJ, 158, 143
Hippke, M. & Heller, R. 2019, A&A, 623, A39
Hollands, M. A., Gänsicke, B. T., & Koester, D. 2018, MNRAS, 477, 93
Howard, A. W., Marcy, G. W., Bryson, S. T., et al. 2012, ApJS, 201, 15
Howell, S. B., Sobeck, C., Haas, M., et al. 2014, PASP, 126, 398
Hoyer, S., Guterman, P., Demangeon, O., et al. 2020, A&A, 635, A24
Iben, Icko, J. 1990, ApJ, 353, 215
Jehin, E., Gillon, M., Queloz, D., et al. 2011, The Messenger, 145, 2
Jones, M. I., Wittenmyer, R., Aguilera-Gómez, C., et al. 2020, arXiv e-prints, arXiv:2006.01277
Kennedy, G. M., Hope, G., Hodgkin, S. T., & Wyatt, M. C. 2019, MNRAS, 482, 5587
Kostov, V. B., Schlieder, J. E., Barclay, T., et al. 2019, AJ, 158, 32
Kovács, G., Zucker, S., & Mazeh, T. 2002, A&A, 391, 369
Krzesinski, J. 2015, A&A, 581, A7
Lee, J. W., Kim, S.-L., Kim, C.-H., et al. 2009, AJ, 137, 3181
Lutz, R., Schuh, S., & Silvotti, R. 2012, Astronomische Nachrichten, 333, 1099
Mackebrandt, F., Schuh, S., Silvotti, R., et al. 2020, A&A, 638, A108
Maldonado, R. F., Villaver, E., Mustill, A. J., Chávez, M., & Bertone, E. 2021, MNRAS, 501, L43
Marsh, T. R. 2018, Circumbinary Planets Around Evolved Stars, ed. H. J. Deeg & J. A. Belmonte, 96
Maxted, P. f. L., Heber, U., Marsh, T. R., & North, R. C. 2001, MNRAS, 326, 1391
Mayor, M., Marmier, M., Lovis, C., et al. 2011, arXiv e-prints, arXiv:1109.2497
Miglio, A., Brogaard, K., Stello, D., et al. 2012, MNRAS, 419, 2077
Miller Bertolami, M. M., Althaus, L. G., Unglaub, K., & Weiss, A. 2008, A&A, 491, 253
Mosser, B., Goupil, M. J., Belkacem, K., et al. 2012, A&A, 548, A10
Mustill, A. J., Veras, D., & Villaver, E. 2014, MNRAS, 437, 1404
Mustill, A. J., Villaver, E., Veras, D., Gänsicke, B. T., & Bonsor, A. 2018, MNRAS, 476, 3939
Norris, J. M., Wright, J. T., Wade, R. A., Mahadevan, S., & Gettel, S. 2011, ApJ, 743, 88
Nowak, G., Luque, R., Parviainen, H., et al. 2020, A&A, 642, A173
Østensen, R. H., Silvotti, R., Charpinet, S., et al. 2011, MNRAS, 414, 2860
Østensen, R. H., Silvotti, R., Charpinet, S., et al. 2010, MNRAS, 409, 1470
Pablo, H., Kawaler, S. D., & Green, E. M. 2011, ApJ, 740, L47
Pelisoli, I., Vos, J., Geier, S., Schaffenroth, V., & Baran, A. S. 2020, A&A, 642, A180
Pozuelos, F. J., Suárez, J. C., de Elía, G. C., et al. 2020, A&A, 641, A23
Pulley, D., Faillace, G., Smith, D., Watkins, A., & Owen, C. 2015, Journal of the British Astronomical Association, 125, 284
Qian, S. B., Zhu, L. Y., Dai, Z. B., et al. 2012, ApJ, 745, L23
Quinn, S. N., Becker, J. C., Rodriguez, J. E., et al. 2019, AJ, 158, 177
Rappaport, S., Levine, A., Chiang, E., et al. 2012, ApJ, 752, 1
Ratzloff, J. K., Barlow, B. N., Kupfer, T., et al. 2019, ApJ, 883, 51
Reindl, N., Geier, S., Kupfer, T., et al. 2016, A&A, 587, A101
Ricker, G. R., Winn, J. N., Vanderspek, R., et al. 2014, in Society of Photo-Optical Instrumentation Engineers (SPIE) Conference Series, Vol. 9143, Space Telescopes and Instrumentation 2014: Optical, Infrared, and Millimeter Wave, 914320
Saffer, R. A., Bergeron, P., Koester, D., & Liebert, J. 1994, ApJ, 432, 351
Saio, H. & Jeffery, C. S. 2000, MNRAS, 313, 671
Saio, H. & Jeffery, C. S. 2002, MNRAS, 333, 121
Sanchis-Ojeda, R., Rappaport, S., Pallè, E., et al. 2015, ApJ, 812, 112
Sato, B., Toyota, E., Omiya, M., et al. 2008, PASJ, 60, 1317
Schaffenroth, V., Barlow, B. N., Geier, S., et al. 2019, A&A, 630, A80
Schaffenroth, V., Casewell, S. L., Schneider, D., et al. 2021, MNRAS, 501, 3847
Schaffenroth, V., Geier, S., Heber, U., et al. 2018, A&A, 614, A77
Schleicher, D. R. G. & Dreizler, S. 2014, A&A, 563, A61
Schneider, D., Heber, U., Geier, S., Latour, M., & Irrgang, A. 2019, 10.5281/zenodo.3428841
Silvotti, R., Charpinet, S., Green, E., et al. 2014, A&A, 570, A130
Silvotti, R., Ostensen, R. H., & Telting, J. H. 2020, arXiv e-prints, arXiv:2002.04545
Silvotti, R., Schuh, S., Janulis, R., et al. 2007, Nature, 449, 189
Silvotti, R., Schuh, S., Kim, S. L., et al. 2018, A&A, 611, A85
Sowicka, P., Handler, G., Dębski, B., et al. 2017, MNRAS, 467, 4663
Stark, M. A. & Wade, R. A. 2003, AJ, 126, 1455
Stassun, K. G., Oelkers, R. J., Paegert, M., et al. 2019, AJ, 158, 138
Van Eylen, V., Albrecht, S., Gandolfi, D., et al. 2016, AJ, 152, 143
Van Grootel, V., Charpinet, S., Brassard, P., Fontaine, G., & Green, E. M. 2013, A&A, 553, A97
van Sluijs, L. & Van Eylen, V. 2018, MNRAS, 474, 4603
Vanderburg, A., Johnson, J. A., Rappaport, S., et al. 2015, Nature, 526, 546
Vanderburg, A., Rappaport, S. A., Xu, S., et al. 2020, Nature, 585, 363
Veras, D. & Fuller, J. 2020, MNRAS, 492, 6059
Völschow, M., Banerjee, R., & Hessman, F. V. 2014, A&A, 562, A19
Vos, J., Németh, P., Vučković, M., Østensen, R., & Parsons, S. 2018, MNRAS, 473, 693
Wahl, S. M., Hubbard, W. B., Militzer, B., et al. 2017, Geophys. Res. Lett., 44, 4649
Webbink, R. F. 1984, ApJ, 277, 355
Welsh, W. F., Orosz, J. A., Carter, J. A., et al. 2012, Nature, 481, 475
Wilson, T. G., Farihi, J., Gänsicke, B. T., & Swan, A. 2019, MNRAS, 487, 133
Wittenmyer, R. A., Horner, J., & Marshall, J. P. 2013, MNRAS, 431, 2150
Zhang, X. & Jeffery, C. S. 2012, MNRAS, 419, 452
Zhu, L.-Y., Qian, S.-B., Fernández Lajús, E., Wang, Z.-H., & Li, L.-J. 2019, Research in Astronomy and Astrophysics, 19, 134
Zorotovic, M. & Schreiber, M. R. 2013, A&A, 549, A95

[1] Space sciences, Technologies and Astrophysics Research (STAR) Institute, Université de Liège, 19C Allée du 6 Août,

B-4000 Liège, Belgium
e-mail: valerie.vangrootel@uliege.be
[2] Astrobiology Research Unit, Université de Liège, Allée du 6 Août 19C, B-4000 Liège, Belgium
[3] Institut de Recherche en Astrophysique et Planétologie, CNRS, Université de Toulouse, CNES, 14 avenue Edouard Belin, F-31400 Toulouse, France
[4] Observatoire Astronomique de l'Université de Genève, Chemin Pegasi 51, Versoix, Switzerland
[5] Physikalisches Institut, University of Bern, Gesellsschaftstrasse 6, 3012 Bern, Switzerland
[6] Center for Space and Habitability, Gesellsschaftstrasse 6, 3012 Bern, Switzerland
[7] Aix Marseille Univ, CNRS, CNES, LAM, Marseille, France
[8] Instituto de Astrofísica e Ciências do Espaço, Universidade do Porto, CAUP, Rua das Estrelas, 4150-762 Porto, Portugal
[9] Department of Physics, High Point University, One University Parkway, High Point, NC 27268
[10] Universidad Internacional de Valencia (VIU), Carrer del Pintor Sorolla 21, 46002, Valencia, Spain
[11] Dpto. Física Teórica y del Cosmos, Universidad de Granada, 18071, Granada, Spain
[12] Department of Physics, Astronomy and Materials Science, Missouri State University, 901 S. National, Springfield, MO 65897, USA
[13] Instituto de Astrofísica de Canarias, 38200 La Laguna, Tenerife, Spain
[14] Departamento de Astrofísica, Universidad de La Laguna, 38206 La Laguna, Tenerife, Spain
[15] Institut de Ciències de l'Espai (ICE, CSIC), Campus UAB, Can Magrans s/n, 08193 Bellaterra, Spain
[16] Institut d'Estudis Espacials de Catalunya (IEEC), 08034 Barcelona, Spain
[17] ESTEC, European Space Agency, 2201AZ, Noordwijk, NL
[18] Depto. de Astrofísica, Centro de Astrobiologia (CSIC-INTA), ESAC campus, 28692 Villanueva de la Cãda (Madrid), Spain
[19] Departamento de Física e Astronomia, Faculdade de Ciências, Universidade do Porto, Rua do Campo Alegre, 4169-007 Porto, Portugal
[20] Space Research Institute, Austrian Academy of Sciences, Schmiedlstrasse 6, A-8042 Graz, Austria
[21] Université Grenoble Alpes, CNRS, IPAG, 38000 Grenoble, France
[22] Department of Astronomy, Stockholm University, AlbaNova University Center, 10691 Stockholm, Sweden
[23] INAF, Osservatorio Astrofisico di Catania, Via S. Sofia 78, 95123 Catania, Italy
[24] Admatis, Miskok, Hungary
[25] Institute of Planetary Research, German Aerospace Center (DLR), Rutherfordstrasse 2, 12489 Berlin, Germany
[26] Centre for Exoplanet Science, SUPA School of Physics and Astronomy, University of St Andrews, North Haugh, St Andrews KY16 9SS, UK
[27] Université de Paris, Institut de physique du globe de Paris, CNRS, F-75005 Paris, France
[28] Lund Observatory, Dept. of Astronomy and Theoretical Physics, Lund University, Box 43, 22100 Lund, Sweden
[29] Leiden Observatory, University of Leiden, PO Box 9513, 2300 RA Leiden, The Netherlands
[30] Department of Space, Earth and Environment, Chalmers University of Technology, Onsala Space Observatory, 43992 Onsala, Sweden
[31] Dipartimento di Fisica, Università degli Studi di Torino, via Pietro Giuria 1, I-10125, Torino, Italy
[32] University of Vienna, Department of Astrophysics, Türkenschanzstrasse 17, 1180 Vienna, Austria
[33] Department of Physics, University of Warwick, Gibbet Hill Road, Coventry CV4 7AL, United Kingdom
[34] Konkoly Observatory, Research Centre for Astronomy and Earth Sciences, 1121 Budapest, Konkoly Thege Miklós út 15-17, Hungary
[35] ELTE Eötvös Loránd University, Institute of Physics, Pázmány Péter sétány 1/A, 1117 Budapest, Hungary
[36] Sydney Institute for Astronomy, School of Physics A29, University of Sydney, NSW 2006, Australia
[37] IMCCE, UMR8028 CNRS, Observatoire de Paris, PSL Univ., Sorbonne Univ., 77 av. Denfert-Rochereau, 75014 Paris, France
[38] Institut d'astrophysique de Paris, UMR7095 CNRS, Université Pierre & Marie Curie, 98bis blvd. Arago, 75014 Paris, France
[39] INAF, Osservatorio Astronomico di Padova, Vicolo dell'Osservatorio 5, 35122 Padova, Italy
[40] Astrophysics Group, Keele University, Staffordshire, ST5 5BG, United Kingdom
[41] Institute of Optical Sensor Systems, German Aerospace Center (DLR), Rutherfordstrasse 2, 12489 Berlin, Germany
[42] Dipartimento di Fisica e Astronomia, Università degli Studi di Padova, Vicolo dell'Osservatorio 3, 35122 Padova, Italy
[43] Centre Spatial de Liège, STAR institute, Université de Liège, avenue du Pré Aily, B-4031 Angleur (Liège), Belgium
[44] Cavendish Laboratory, JJ Thomson Avenue, Cambridge CB3 0HE, UK
[45] Center for Astronomy and Astrophysics, Technical University Berlin, Hardenberstrasse 36, 10623 Berlin, Germany
[46] Institut für Geologische Wissenschaften, Freie Universität Berlin, 12249 Berlin, Germany
[47] INAF-Osservatorio Astrofisico di Torino, Strada dell'Osservatorio 20, 10025 Pino Torinese, Italy
[48] ELTE Eötvös Loránd University, Gothard Astrophysical Observatory, 9700 Szombathely, Szent Imre h. u. 112, Hungary
[49] MTA-ELTE Exoplanet Research Group, 9700 Szombathely, Szent Imre h. u. 112, Hungary
[50] Institute of Astronomy, University of Cambridge, Madingley Road, Cambridge, CB3 0HA, United Kingdom

Appendix A: List of hot subdwarfs observed in the original Kepler field

Table A.1.

Appendix B: List of hot subdwarfs observed in the K2 fields

Table B.1.

Table A.1. List of hot subdwarfs observed in the original Kepler field*.

KIC	Class	Other name	Kp	Quarters (SC)	Quarters (LC)
sdB pulsators					
9472174	sdB+dM	2M1938+4603	12.3	Q0, Q5-Q17.2	All: Q0-Q17.2
2437937	sdB	B5 (NGC6791)	13.9	Q11.X	Q11
3527751	sdB	J19036+3836	14.8	Q2, Q5-Q17.2	Idem SC
11558725	sdB+WD	J19265+4930	14.9	Q3.3, Q6-Q17.2	Q3, Q5-Q17.2
5807616	sdB	KPD 1943+4058	15.0	Q2.3, Q5-Q17.2	Idem SC
10553698	sdB	J19531+4743	15.1	Q4.1, Q8-Q10, Q12-Q14, Q16-Q17.2	Q4-Q6, Q8-Q10, Q12-Q17.2
2697388	sdB	J19091+3756	15.4	Q2.3, Q5-Q17.2	Idem SC
7668647	sdB+WD	FBS1903+432	15.4	Q3.1, Q6-Q17.2	Q3.1, Q5-Q17.2
10001893	sdB	J19095+4659	15.8	Q3.2, Q6-Q17.2	Q3.2, Q5-Q17.2
10139564	sdB	J19249+4707	16.1	Q2.1, Q5-Q17.2	Idem SC
8302197	sdB	J19310+4413	16.4	Q3.1, Q5-Q17.2 except Q12	idem SC
7664467	sdB	J18561+4319	16.4	Q2.3, Q5-Q17.2 except Q12	idem SC
10670103	sdB	J19346+4758	16.5	Q2.3, Q5-Q17.2	Idem SC
11179657	sdB+dM	J19023+4850	17.1	Q2.3, Q5-Q17.2 except Q8 and Q12	idem SC
2991403	sdB+dM	J19272+3808	17.1	Q1, Q5-Q17.2	Idem SC
2991276	sdB	J19271+3810	17.4	Q2.1, Q6-Q17.2 except Q12	Idem SC
2569576	sdB	B3 (NGC6791)	18.1	Q11.3, Q14-Q17.2	Q11, Q14-Q17.2
2438324	sdB+dM	B4 (NGC6791)	18.3	Q6-Q17.2	Idem SC
sdB/sdOB non pulsators					
6848529	sdB+?	BD +42 3250	10.7	Q0	All: Q0-Q17.2
1868650	sdB+dM	KBS 13	13.4	Q1	All: Q0-Q17.2
9543660	sdOB		13.8	Q1	Q1-Q17, except Q7 and Q11
10982905	sdB+F/G	J19405+4827	14.1	Q2.1	Q2-Q10
6188286	sdOB		14.2	Q2.3	Q2, Q6-Q8, Q14-Q16
8054179	He-sdOB		14.4	Q3.1, Q6	Q3.1, Q4-Q17.2 except Q11 and Q12
7975824	sdOB+WD	KPD 1946+4340	14.6	Q1, Q5-Q12	Q1, Q5-Q17.2
10449976	He-sdOB		14.9	Q3.2	Q3, Q5-Q9
3353239	sdB		15.2	Q4.1	Q4-Q5, Q7-Q9, Q13-Q17
10593239	sdB+F/G	J19162+4749	15.3	Q2.3	Q2, Q5-Q17.2
2569583	sdB	B6 (NGC6791)	15.4	Q11.2	Q11
7104168	sdB		15.5	Q3.1	Q3, Q5-Q9
10149211	sdB+?		15.5	Q4.2	Q4-Q17.2
10789011	sdOB		15.5	Q3.2	Q3, Q5-Q10
11350152	sdB+F/G		15.5	Q3.1	Q3, Q5-Q10
7434250	sdB+?	J19135+4302	15.5	Q2.3	Q2, Q5-Q17.2
2020175	sdB		15.5	Q3.1	Q3, Q5-Q10, Q13-Q17.2
12021724	sdB+WD?		15.6	Q4.2	Q4-Q10
3343613	He-sdOB		15.7	Q3.2	Q3, Q5-Q10
5938349	sdB		16.1	Q3.2	Q3, Q10
6614501	sdB+WD?		16.1	Q3.3, Q5, Q6, Q8-Q10	Q3.3, Q5-Q17.2
9211123	sdB		16.1	Q3.3	Q3, Q5-Q10, Q13-Q17.2
9957741	He-sdOB		16.1	Q2.1	Q2, Q6-Q9
2304943	sdB		16.2	Q3.3	Q3, Q10
8496196	sdOB		16.4	Q2.3	Q2, Q6-Q10
8874184	sdB+?		16.5	Q4.1	Q4-Q10, Q13-Q17.2
8022110	sdB		16.5	Q2.3	Q2, Q6-Q10, Q13-Q17.2
6878288	He-sdOB+?		16.7	Q3.1	Q3, Q5-Q10
6522967	sdB		16.9	Q3.2	Q3, Q10
7799884	sdB		16.9	Q4.1	Q4.1
10462707	sdB+WD?		16.9	Q4.1	Q4.1, Q10
11400959	sdB		16.9	Q4.1	Q4.1
10784623	sdB		17.0	Q10	Q4-Q10 except Q8
10961070	sdOB		17.0	Q4.2	Q4.2
3527028	sdB+?		17.1	Q4.2	Q4-Q10
5340370	sdB+?		17.1	Q4.2	Q4, Q10
9569458	sdB		17.2	Q1	Q1
8889318	sdB		17.2	Q2.3	Q2.3, Q13-Q17.2
9408967	He-sdOB		17.2	Q2.3	Q2.3, Q10
4244427	sdB		17.3	Q2.1, Q6-Q10	Q2.1, Q6-Q17.2 except Q12
8142623	sdB+?	J18427+4404	17.3	Q1	Q1, Q5-Q17.2
11357853	sdOB		17.4	Q2.1	Q2.1
3527617	He-sdOB		17.5	Q2.2	Q2.2
3729024	sdB		17.6	Q2.2	Q2.2
9095594	sdB		17.7	Q3.2	Q3.2
5342213	sdOB		17.7	Q2.2	Q2.2, Q14-Q16
10661778	sdB		17.7	Q2.3, Q6-Q10	Q2.3, Q6-Q17.2 except Q11 and Q12
sdO non pulsators					
7755741	sdO		13.7	Q1	Q1-Q17
9822180	sdO+F/G		14.6	Q2.1, Q6	Q2.1, Q6-Q10
7353409	sdO		14.7	Q2.2, Q5	Q2.2, Q5-Q9
10207025	He-sdO		15.0	Q3.3	Q3.3, Q5-Q9
7335517	sdO+dM		15.7	Q3.2, Q6	Q3.2, Q5-Q17.2
2297488	sdO+F/G		17.2	Q1	Q1
2303576	He-sdO+?		17.4	Q3.3, Q6	Q3.3, Q6-Q17.2

*Commissioning (9.7 days starting 2 May 2009): Q0; Survey phase: Q1: 33.5 d (12 May-14 June 2009), Q2, Q3, and Q4: about 90 days each, divided in 3, i.e. monthly surveys; Rest of the mission: Q5 to Q16: about 90 days each; mission stopped at Q17.2 (11 May 2013).

Table B.1. List of hot subdwarfs observed in the K2 fields†.

KIC	Class	Other name	Kp	Campaign (SC)	Campaign (LC)
sdB pulsators					
220641886	sdB	HD 4539	10.40	8	8
228755638	sdB+dM	HW Vir	10.76	10 (101-102)	10 (101-102)
211623711	He-sdB	UVO 0825+15	11.89	5;18	5;18
220376019	sdB+WD	PG 0101+039	12.11	8	8
220422705	sdB+G	PG 0039+049	12.87	8	8
249942493	sdB	EC 15103-1557	12.89	15	15
211779126	sdB	2M0856+1701	12.92	5;18	5;18
246387816	sdB+dM	EQ Psc	12.92	12	12
246023959	sdB+dM	PHL 457	13.04	12	12
211881419	iHe-sdB	PG 0848+186	13.30	16;18	5;16;18
201203416	sdB	PG 1156-037	13.46	10 (101-102)	10 (101-102)
248411044	sdB	UY Sex	13.56	14	14
246141920	sdB	PHL 531	13.99	12	12
211433013	sdB+WD	LT Cnc	14.02	16	16
211765471	sdB+WD	HZ Cnc	14.04	5;16;18	5;16;18
220614972	sdB+F	PG 0048+091	14.29	8	8
211392098	sdB+MS	SDSS J082517.99+113106.3	14.34	18	5;18
211437457	sdB	PG 0902+124	14.73	16	16
246683636	sdB+dM	V1405 Ori	15.07	13	13
248368659	sdB+WD	VPHAS J181343.0-213843.9	15.10	9 (91-92)	9 (91-92)
212508753	sdB+F7	PG 1315-123	15.13	6;17	6;17
211823779	sdB+F1	SDSS J082003.35+173914.2	15.22	5;18	5;18
212475716	sdB+MS	EC 13356-1300	15.24	17	17
211696659	sdB+WD	SDSS J083603.98+155216.4	15.50	5;18	5;18
212707862	sdB	SDSS J135544.71-080354.3	15.55	6;17	6;17
212204284	sdB	PG 0843+246	15.64	16	16
246283223	sdB	HE 2307-0340	15.66	12	12
248368658	sdB		15.70	9 (91-92)	9 (91-92)
218717602	sdB		15.76	7	7
211938328	sdB+F6	LB 378	15.78	5;18	5;18
218366972	sdB+WD		15.94	7	7
201206621	sdB+WD	PG 1142-037	15.99	1	1
212487276	sdB	EC 13359-1245	16.23	17	17
217280630	sdB		16.33	7	7
215776487	sdB		16.35	7	7
203948264	sdB		16.70	2	2
246373305	iHe-sdB	PHL 417	16.88	12	12
251668197	sdB	EC 15094-1725	17.00	15	15
229002689	sdB	SDSS J122057.48-012642.3	18.65	10 (101-102)	10 (101-102)
220188903	sdB+WD	PB 6373	14.91	no data	8
230195595	sdB		15.59	no data	11
sdB/sdOB non pulsators, single					
234319842	sdB		12.97	11 (111-112)	11 (111-112)
60017832	sdB	PG 2349+002	13.27	T	
211708181	sdB	GALEX J081233.6+160121	13.77	5	5
227389858	sdB		13.79	11 (111-112)	11 (111-112)
246230928	sdB	PHL 529	13.93	12	12
206535752	sdB	PHL 358	13.99	3	3
201648341	sdB	PG 1214+031	14.04	10 (101-102)	10 (101-102)
217204898	sdB		14.26	7	7
246643895	sdB	HS 0446+1344	14.50	13	13
212722777	sdB	PG 1330-074	14.93	17	17
211727748	sdB	PG 0838+165	14.99	5;16	5;16
206073023	sdB	BPS CS 29512-38	15.00	3	3
210837690	sdB		15.11	4	4
212498842	sdB	EC 13162-1229	15.26	6	6
212465180	sdB	EC 13265-1313	15.56	6	6
212160066	sdB	SDSS J082445.68+231520.3	15.57	18	5;18
246901153	sdB	KUV 04369+1640	15.70	13	13
249601610	sdB	EC 15050-2017	15.71	15	15
246980092	sdB	KUV 04482+1727	15.74	13	13
218148570	sdB		15.74	7	7
228914323	sdB	PG 1249-028	15.76	10 (101-102)	10 (101-102)
228682488	sdB	SDSS J085217.70+211637.4	16.00	16	16

Table B.1. (Continued).

KIC	Class	Other name	Kp	Campaign (SC)	Campaign (LC)
212818294	sdB	PG 1356-047	16.15	6;17	6;17
248422838	sdB	PG 1032+007	16.27	14	14
214515136	sdB		16.30	7	7
251603936	sdB	SDSS J131916.15-011405.0	16.69	17	17
201531672	sdB	SDSS J112757.48+010044.2	16.89	1	1
251457058	sdB	SDSS J105428.85+010514.7	17.10	14	14
246371369	sdB	PB 5212	17.11	12	12
211552072	sdB	SDSS J084556.85+135211.3	17.50	16	16
212567176	sdB	HE 1309-1102	17.65	6	6
249585191	sdB	EC 15064-2029	17.95	15	15
248840987	sdB	SDSS J102050.99+114024.3	18.15	14	14
248810568	sdOB	SDSS J110055.94+105542.3	14.22	14	14
246997679	sdOB	KUV 05109+1739	14.58	13	13
211421561	sdOB	SDSS J090042.68+115749.9	14.90	16	16
220265912	sdOB	PG 0055+016	15.19	8	8
249700050	sdOB	EC 15059-1902	15.65	15	15
206240954	sdOB	SDSS J220337.88-090733.5	16.31	3	3
210731139	sdOB	SDSS J032427.24+184918.2	16.37	4	4
246087406	sdOB	PB 7470	16.46	12	12
206186190	sdOB	BPS CS 22886-65	16.49	3	3
251605347	sdOB	SDSS J133611.02-011156.0	18.69	17	17
246745570	He-sdB	KUV 04456+1502	15.68	13	13
211920209	He-sdB	PG 0850+192	16.39	18	5; 16; 18
249770424	He-sdOB	GALEX J152332.2-181726	14.00	15	15
211495446	He-sdOB	PG 0838+133	14.03	5;16	5;16
248748173	He-sdOB	PG 1033+097	16.38	14	14
248761152	He-sdOB	PG 1045+100	17.09	14	14
248915544	He-sdOB	SDSS J103806.64+134412.1	17.21	14	14
211841249	sdB	SDSSJ082734.96+175356.0	14.64	5;18	5;18
250083298	sdB	EC15203-1418	17.34	15	15
sdB/sdOB non pulsators, in binaries					
220468352	sdB+F	PB 6355	13.01	8	8
251377113	sdB+F/G	SDSS J090827.24+231417.9	13.53	16	16
211499370	sdB+F/G/K	SDSS J082556.80+130753.5	14.60	5	5;18
218637228	sdB+F/G		14.79	7	7
227441033	sdB+F/G		15.10	11 (111-112)	11 (111-112)
216924452	sdB+F/G		15.53	7	7
250121838	sdB+F/G/K	EC 15365-1350	15.74	15	15
246151922	sdB+G9	HE 2322-0617	15.74	12;19	12;19
212630158	sdB+F/G		15.75	6	6
246868556	sdB+F/G	GALEX J050252.2+162647	15.78	13	13
246864591	sdB+F/G/K	KUV 04571+1620	15.98	13	13
211910684	sdB+F/G	PG 0906+191	15.99	16	16
212108396	sdB+F/G	SDSS J082447.30+221112.9	16.02	5	5;18
211400847	sdB+F/G	SDSS J084447.00+113910.0	16.43	5	5;18
212003762	sdB+F/G	SDSS J081406.79+201901.7	16.51	18	18
212137838	sdB+F/G	Ton 920	16.54	5	5
250152590	sdB+F/G/K	LB 889	17.13	15	15
248467942	sdB+F/G	SDSS J103022.07+020524.3	17.24	14	14
211732575	sdB+F/G	SDSS J082426.51+162145.1	17.68	18	18
251583165	sdB+F/G	SDSS J131932.19-014131.2	18.24	17	17
212866280	sdB+F/G	SDSS J133701.51-031732.2	18.27	17	17
212410755	sdB+WD	EC 13332-1424	13.46	6	6
201535046	sdB+?	PG 1049+013	14.44	14	14
251372905	sdOB+F/G	SDSS J091216.06+225452.7	15.30	16	16
211904152	sdOB+F/G	PG 0912+189	15.93	16	16
248767552	sdOB+WD?	SDSS J101833.11+095336.1	14.97	14	14
246877984	sdOB+WD	KUV 05053+1628	16.11	13	13
sdO non pulsators					
212762631	sdO	PG 1355-064	13.76	6	6;17
220179214	sdO	GD 934	14.93	8	8
248520995	sdO	SDSS J110053.55+034622.8	17.25	14	14
211517387	sdO	SDSS J082944.74+132302.5	17.32	5	5
249862817	sdO	EC 15447-1656	18.05	15	15
228821386	He-sdO	PG 1220-056	14.86	10 (101-102)	10 (101-102)

Table B.1. (Continued).

KIC	Class	Other name	Kp	Campaign (SC)	Campaign (LC)
249867379	He-sdO	EC 15348-1652	15.35	15	15
205247324	He-sdO		16.01	2	2
201640895	He-sdO	SDSS J110215.45+024034.2	17.60	14	14
228960704	He-sdO	SDSS J123821.48-021211.4	18.49	10 (101-102)	10 (101-102)
Misc., in LC only					
201150341	sdB	HE 1140-0500	14.50	no data	1
214958569	sdB		15.70	no data	7
216775790	sdB		16.50	no data	7
201236182	sdB	PG 1154-031	16.59	no data	1
211720816	sdB	SDSS J083901.50+161148.0	16.71	no data	5; 16; 18
211594465	sdB	SDSS J081931.22+142756.1	17.19	no data	5; 18
248912731	sdB	SDSS J103832.41+133848.3	17.44	no data	14
201201339	sdB	SDSS J112757.48+010044.2	17.50	no data	1
201590024	sdB	SDSS J113418.00+015322.1	17.65	no data	1
201698091	sdB	SDSS J114821.29+033625.7	17.70	no data	1
229021782	sdB	SDSS J125410.86-010408.3	17.72	no data	10
228682339	sdB	SDSS J082824.20+212556.7	17.73	no data	5; 16; 18
251457060	sdB	SDSS J104725.10+010847.2	17.80	no data	14
248783069	sdB	SDSS J104620.14+101629.7	18.65	no data	14
251410019	sdB	SDSS J085809.09+252134.6	18.87	no data	16
201424163	sdB+WD	PG 1136-003	15.96	no data	1
228682347	sdB+WD	SDSS J083139.68+162316.4	17.91	no data	5
248783744	sdB+WD	SDSS J103218.40+101725.8	18.82	no data	14
211460944	sdB+WD ?	SDSS J084556.85+135211.3	15.36	no data	16
228796212	sdB	SDSS J124446.64-065625.8	18.83	no data	10
211991114	sd+F/G	Ton 914	15.10	no data	5; 18
211930840	He-sdB	SDSS J091512.06+191114.6	19.13	no data	16
201734164	sdOA	PG 1110+045	14.84	no data	1
213545287	sdOB	GALEX J191509.0-290311	15.00	no data	7
201924421	sdOB	SDSS J113218.41+075103.0	17.20	no data	1
228682323	sdOB	SDSS J082110.89+183924.1	17.84	no data	5
212034957	sdOB	SDSS J090302.39+205008.9	18.62	no data	16
215669184	He-sdOB	GALEX J193323.6-234553	15.00	no data	7
201802867	He-sdOB	SDSS J111633.29+052507.9	17.80	no data	1
251383153	He-sdOB	SDSS J091044.90+234044.6	18.27	no data	16
229155531	He-sdOB	SDSS J121643.72+020835.9	18.73	no data	10
251357585	He-sdOB	SDSS J092245.79+214238.9	19.01	no data	16
211602914	sd	SDSS J082959.28+143441.8	15.64	no data	5; 18
213716821	sdO	GALEX J192041.4-282939	13.40	no data	7
246735349	He-sdO	KUV 04402+1455	13.97	no data	13
214453765	sdO	GALEX J191158.1-262712	15.30	no data	7
216452306	He-sdO		16.40	no data	7
231422890	sdO		17.07	no data	11
201418759	sdO	SDSS J111438.57-004024.3	18.10	no data	1
201843731	sdO	SDSS J115009.48+061042.1	18.10	no data	1
211559083	sdO	SDSS J084421.10+135807.6	18.18	no data	16
228682365	He-sdO	SDSS J083747.23+194955.9	18.60	no data	5
216747137	sdO+dM	2MASS J18521800-2147506	13.87	no data	7
217750936	sdO+dM		16.70	no data	7

[†]T: Engineering test from 4 to 13 Feb 2014; Campaign 0 (8 March-27 May 2014) to 18 (12 May - 2 July 2018), https://keplerscience.arc.nasa.gov/k2-fields.html

Appendix C: List of hot subdwarfs observed in TESS primary mission

i.e., Sector 1 to 26. https://github.com/franpoz/Hot-Subdwarfs-Catalogues

Appendix D: List of hot subdwarfs observed in TESS extended mission

Sector 27 to Sector 32. https://github.com/franpoz/Hot-Subdwarfs-Catalogues